

THE STATIC CONDENSATION REDUCED BASIS ELEMENT METHOD FOR A MIXED-MEAN CONJUGATE HEAT EXCHANGER MODEL*

SYLVAIN VALLAGHÉ[†] AND ANTHONY T. PATERA[†]

Abstract. We propose a new approach for the simulation of conjugate heat exchangers. First, we introduce a dimensionality-reduced mathematical model for conjugate (fluid-solid) heat transfer: in the fluid channels, we consider a mixed-mean temperature defined on one-dimensional filaments; in the solid we consider a detailed partial differential equation conduction representation. We then propose a Petrov–Galerkin finite element (FE) numerical approximation which provides suitable stability and accuracy for our mathematical model. We next apply the static condensation reduced basis element (scRBE) method: a domain synthesis approach with parametric model order reduction at the intradomain level to populate a Schur complement at the interdomain level. We first build a library of “components,” each corresponding to a subdomain with a simple fluid channel geometry; for each component, we prepare Petrov–Galerkin reduced basis bubble approximations (and error bounds). We then assemble the system equations by static condensation and solve for the temperature distribution in the full domain. System-level error bounds are derived from matrix perturbation arguments; we also introduce a new output error bound which is sharper than the original scRBE estimator. We present numerical results for a two-dimensional automotive radiator model which demonstrate the flexibility, accuracy, and computational efficiency of our approach.

Key words. reduced basis, conjugate heat transfer, domain decomposition, a posteriori error estimation

AMS subject classifications. 65N12, 65N15, 65N30, 65N55

DOI. 10.1137/120887709

1. Introduction. Heat exchangers are designed to improve the heat transfer between fluid streams. Perhaps the most common application is automotive radiators: engine coolant passes through an exchanger to discharge heat to external flowing air. It is important to be able to predict the performance of a heat exchanger in order to develop effective designs. Some analytical methods, such as the log-mean temperature difference (LMTD) and the number of transfer units (NTU) approaches [17] permit calculation of the total heat transferred within a heat exchanger. However, both methods require estimation of the overall heat transfer coefficient and exchange area; the former, in particular, can be quite difficult to predict with any accuracy.

A more refined analysis of a heat exchanger hence requires a conjugate heat transfer model which incorporates the thermal interactions between the constituent solid and fluid elements. The simplest situation is a fluid flow in a straight channel with walls of constant thickness; in this case, the conjugate heat transfer problem can be readily solved analytically. However, in more realistic configurations with more complex channels and, in particular, finned solid surfaces—such as automotive radiators—numerical approaches must be invoked [1, 8, 21, 26]. The latter are quite expensive and typically preclude interactive or conceptual design. In this paper we consider a compromise between NTU flexibility and conjugate fidelity. In particu-

*Submitted to the journal’s Computational Methods in Science and Engineering section August 10, 2012; accepted for publication (in revised form) November 19, 2013; published electronically May 6, 2014. This work was supported by ONR grant N00014-11-0713.

<http://www.siam.org/journals/sisc/36-3/88770.html>

[†]Department of Mechanical Engineering, Massachusetts Institute of Technology, Cambridge, MA 02139 (svallagh@mit.edu, patera@mit.edu).

lar, we propose several model order reduction strategies which permit us to rapidly simulate a complete two-dimensional (2D) heat exchanger while still retaining a local description of the thermal interactions between fluid and solid.

In a first stage, we introduce a 2D mathematical model for some simple channel “components” in which we couple the 2D conduction equation in the solid to the one-dimensional (1D) fluid mixed-mean temperature equation in the channel (see [9, 7, 19] for similar heterogeneous dimensionality reduction approaches). Nusselt numbers serve to model the heat transfer between the fluid in the channel and the interior channel walls, and between any external flow and the heat exchanger exterior walls. Note that both the flow rates in the channels and the local Nusselt numbers must be included in the model. We then derive a Petrov–Galerkin finite element (FE) approximation for each of these component models.

In a second stage, we consider an entire heat exchanger system which we synthesize from our simple channel components. For each component type, we introduce several parameters (flow rate, heat transfer coefficients) and perform parametric model order reduction: we replace the FE approximation with a much less expensive reduced basis (RB) approximation [23]. Thanks to the latter, we are able to compute very rapidly the solution over a component for any desired parameter values. To simulate the entire heat exchanger, we first choose parameters for each subdomain and compute the corresponding RB approximations; we then invoke static condensation to assemble these component-level contributions in a complete system description. This approach, denoted the static condensation reduced basis element (scRBE) method and first introduced in [12], may be viewed as a synthesis of two earlier approaches: the reduced basis element method [18] and component modal synthesis [11, 4].

The key contributions of this paper are, first, a dimensionality-reduced mathematical model for heat exchanger components; second, a Petrov–Galerkin FE and RB numerical approximation for these component models; third, a scRBE formulation for heat exchanger systems;¹ and fourth, an improved a posteriori output error bound which can be broadly applied in the scRBE context well beyond our current heat exchanger context.

This paper proceeds as follows. Section 2 provides a complete description of our model for conjugate heat transfer within a single channel component; we also provide the associated Petrov–Galerkin finite element approximation. In section 3, we recall the principles of the RB method and present details for our particular Petrov–Galerkin RB spaces. In section 4, we present some extensions of our model to more complicated channel configurations in which either a single channel splits into two channels or two channels merge into a single channel. In section 5, we present the core of our approach, the scRBE method [12]. Finally, in section 6, we provide numerical results: we start with a simple 1D problem, for which we know the exact solution, in order to compare our approach to a ground truth; we then consider 2D systems, potentially large, corresponding to automotive radiator models.

2. Mathematical model. We consider the heat transfer problem shown in Figure 1: a fluid flows in a plane channel with interior and exterior walls. We do not assume a particular shape for the solid domain Ω ; in practice, the external wall will often be finned to increase the heat transfer with the ambient air. For simplicity, we

¹Our treatment of the heat exchanger does not extend to general transport problems. In particular, the stability is provided by the diffusion in the solid and the nonsmoothness is addressed by a priori knowledge of the mixing locations—a “shock fitting” approach rather than a “shock capturing” approach.

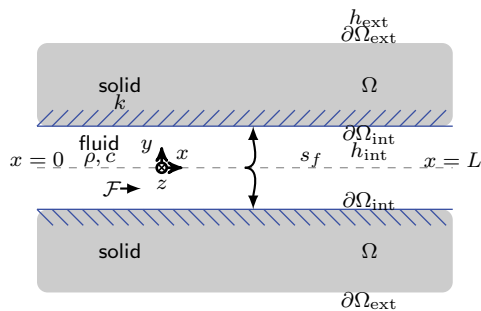


FIG. 1. A channel which comprises fluid $([0, L])$ and solid (Ω) domains.

assume that the geometry and constitutive coefficients are symmetric with respect to the xz plane. Furthermore, we suppose that the material properties are constant in the solid and the fluid, respectively.

The flow is assumed to be independent of the coordinate z . We will consider the fluid bulk temperature, T_b , defined on a 1D filament corresponding to the channel axis (the dashed line in Figure 1); for the bulk temperature we take the mixed-mean temperature [17]. We denote by s_f the filament coordinate; for our simple channel, the filament and solid coordinates are related by the identity mapping $x = s_f$. Following [17], the fluid bulk temperature $T_b(x)$ satisfies

$$\rho c \bar{v} \mathcal{A} \frac{dT_b}{dx} = \mathcal{P} h_{\text{int}} (T_{\partial\Omega_{\text{int}}^{\text{dim}}}(x) - T_b(g(s_f))), \quad 0 \leq x \leq L,$$

where \mathcal{A} is the cross-sectional area of the channel, \mathcal{P} is the perimeter of the channel, ρ is the mass density of the fluid, c is the specific heat of the fluid, \bar{v} is the average flow velocity, and h_{int} is the heat transfer coefficient between the solid and the fluid in the channel. The superscript dim stands for “dimensional,” as we will later nondimensionalize the equations. As a boundary condition, we set $T_b(0) = T_{\text{inlet}}$.

The equation for the solid domain is

$$\begin{cases} -k\Delta T = f_s^{\text{dim}} & \text{in } \Omega^{\text{dim}}, \\ k \frac{\partial T}{\partial n} = h_{\text{ext}}(T_a - T) & \text{on } \partial\Omega_{\text{ext}}^{\text{dim}}, \\ k \frac{\partial T}{\partial n} = h_{\text{int}}(T_b - T) & \text{on } \partial\Omega_{\text{int}}^{\text{dim}}, \end{cases}$$

where Δ is the Laplacian, h_{ext} is the heat transfer coefficient between the solid and the external air, k is the thermal conductivity of the solid, T_a is the external (ambient) air temperature (assumed constant), f_s^{dim} is an optional heat source in the solid domain, and n denotes outward normal.

Note that we will assume that the heat transfer coefficient h_{int} is constant along the channel. Hence this model is most appropriate for turbulent flows which enjoy relatively short development lengths and for which transport is largely dictated by fluid properties and lateral spatial scales [17]. To support this assumption, we refer, for example, to the Gnielinski correlation [10] for the Nusselt number of turbulent flows: the correlation depends only on the Prandtl and Reynolds numbers, which are both constant for a given channel diameter and small temperature variations within the fluid. In particular, and as opposed to correlations for laminar flows, correlations for turbulent flows typically do not depend on the channel wall conditions.

2.1. Nondimensional equations. We define the following dimensionless quantities: $\theta = \frac{T-T_a}{T_{\text{inlet}}-T_a}$; $\phi = \frac{T_b-T_a}{T_{\text{inlet}}-T_a}$; $\xi = \frac{x}{\mathcal{W}}$, where \mathcal{W} is a characteristic length (typically the width of the solid in the y direction); and $\Lambda = \frac{L}{\mathcal{W}}$. We also define $\mathcal{F} = \frac{\rho c \bar{v} A}{\mathcal{P}k}$ (note that k is the conductivity of the solid and hence \mathcal{F} is not a Peclet number), $\text{Bi}_{\text{int}} = \frac{h_{\text{int}}\mathcal{W}}{k}$, and $\text{Bi}_{\text{ext}} = \frac{h_{\text{ext}}\mathcal{W}}{k}$. The equations then become

$$(2.1) \quad \begin{cases} -\Delta\theta = f_s & \text{in } \Omega, \\ \mathcal{F}\frac{d\phi}{d\xi} = \text{Bi}_{\text{int}}(\theta_{\partial\Omega_{\text{int}}} - \phi), & 0 \leq \xi \leq \Lambda, \end{cases}$$

with the boundary conditions

$$(2.2) \quad \begin{cases} \frac{\partial\theta}{\partial\eta} = -\text{Bi}_{\text{int}}(\theta - \phi) & \text{on } \partial\Omega_{\text{int}}, \\ \frac{\partial\theta}{\partial\eta} = -\text{Bi}_{\text{ext}}\theta & \text{on } \partial\Omega_{\text{ext}}, \\ \phi(0) = 1, \end{cases}$$

where η denotes (nondimensional) outward normal. Note $f_s = \frac{f_s^{\text{dim}}\mathcal{W}^2}{k(T_{\text{inlet}}-T_a)}$. As a standard hypothesis, we suppose that $\Lambda > 1$, $\mathcal{F} \geq 2$, $\text{Bi}_{\text{int}} > 0$, and $\text{Bi}_{\text{ext}} > 0$.

2.2. Weak form. We will now introduce a variational formulation for (2.1) and (2.2). To this end, we introduce some functional spaces. For the temperature in the solid, θ , we suppose homogeneous Dirichlet conditions on some part of the boundary $\Sigma \subset \partial\Omega$ such that $\Sigma \cap \partial\Omega_{\text{int}} = \emptyset$ and $\Sigma \cap \partial\Omega_{\text{ext}} = \emptyset$. This subset Σ of the boundary will later correspond to “ports” where “components” can be connected (section 5). Hence we take $\theta \in Y$ for $Y = H^1_{\Sigma}(\Omega) \equiv \{w \in H^1(\Omega) | v|_{\Sigma} = 0\}$, note that $H^1_0(\Omega) \subset Y \subset H^1(\Omega)$ (see [22] for definitions of standard function spaces). For the fluid bulk temperature, ϕ , we take $\phi \in V$ for $V = \{\varphi \in H^1([0, \Lambda]) | \varphi(0) = 0\}$; note that to simplify the presentation we assume that the inhomogeneous boundary condition for the fluid is lifted (and hence we may consider $\phi(0) = 0$). We also define the spaces $W = L^2([0, \Lambda])$, $X = Y \times V$, and $Z = Y \times W$; here X is the trial space such that $w = (\theta, \phi) \in X$, and Z is the test space such that $v = (\vartheta, \varphi) \in Z$. We also define the norms on X and Z ,

$$\begin{aligned} \|w\|_X^2 &\equiv \int_{\Omega} |\nabla\theta|^2 + \int_{[0, \Lambda]} \left(\frac{d\phi}{dx}\right)^2 + \phi^2(\Lambda), \\ \|v\|_Z^2 &\equiv \int_{\Omega} |\nabla\vartheta|^2 + \int_{[0, \Lambda]} \varphi^2. \end{aligned}$$

We are now ready to derive the variational formulation.

We first define the bilinear form $a(\cdot, \cdot)$ on $X \times Z$ such that for $w \in X$ and $v \in Z$,

$$(2.3) \quad \begin{aligned} a(w, v) &= \int_{\Omega} \nabla\theta \nabla\vartheta + \text{Bi}_{\text{ext}} \int_{\partial\Omega_{\text{ext}}} \theta\vartheta \\ &+ \text{Bi}_{\text{int}} \int_{\partial\Omega_{\text{int}}} (\theta - \phi)\vartheta - \text{Bi}_{\text{int}} \int_{\partial\Omega_{\text{int}}} (\theta - \phi)\varphi + \mathcal{F} \int_{[0, \Lambda]} \frac{d\phi}{dx}\varphi. \end{aligned}$$

The bilinear form $a(\cdot, \cdot)$ thus has an obvious affine decomposition with respect to the

parameters $\boldsymbol{\mu} = (\text{Bi}_{\text{ext}}, \text{Bi}_{\text{int}}, \mathcal{F})$,

$$(2.4) \quad a(w, v; \boldsymbol{\mu}) = \sum_{q=0}^Q \theta_q(\boldsymbol{\mu}) a_q(w, v),$$

with $Q = 3$ and $\theta_0(\boldsymbol{\mu}) = 1$, $\theta_1(\boldsymbol{\mu}) = \text{Bi}_{\text{ext}}$, $\theta_2(\boldsymbol{\mu}) = \text{Bi}_{\text{int}}$, $\theta_3(\boldsymbol{\mu}) = \mathcal{F}$. We will suppress for now the dependence of $a(\cdot, \cdot)$ on $\boldsymbol{\mu}$ and reintroduce it later for the reduced basis approximation. We also define the linear form f such that for $v \in Z$,

$$f(v) = \int_{\Omega} f_s v - a(z, v),$$

where $z \in X$ is the lifted inhomogeneous boundary condition at the fluid inlet.

Now taking the scalar product of (2.1) with $v \in Z$, and incorporating the boundary conditions (2.2), we obtain the weak form: find $u \in X$ such that

$$(2.5) \quad a(u, v) = f(v) \quad \forall v \in Z.$$

LEMMA 2.1. *The bilinear form $a(\cdot, \cdot)$ is inf-sup stable and continuous on $X \times Z$.*

Proof. For any $w = (\theta, \phi) \in X$, we define $w^* = (\theta, \phi + \tau \frac{d\phi}{dx}) \in Z$ for some constant τ such that $0 < \tau \leq 1$. Choosing $v = w^*$ in the bilinear form gives

$$\begin{aligned} a(w, w^*) &= \int_{\Omega} |\nabla \theta|^2 + \text{Bi}_{\text{ext}} \int_{\partial\Omega_{\text{ext}}} \theta^2 + \text{Bi}_{\text{int}} \int_{\partial\Omega_{\text{int}}} (\theta - \phi)^2 \\ &\quad - \tau \text{Bi}_{\text{int}} \int_{\partial\Omega_{\text{int}}} \theta \frac{d\phi}{dx} + \tau \mathcal{F} \int_{[0, \Lambda]} \left(\frac{d\phi}{dx} \right)^2 + \frac{1}{2} (\mathcal{F} + \tau \text{Bi}_{\text{int}}) \phi^2(\Lambda). \end{aligned}$$

Using the inequality (for $c \in \mathbb{R}$, $d \in \mathbb{R}$, $\sigma \in \mathbb{R}^+$) $2|c||d| \leq \frac{1}{\sigma} c^2 + \sigma d^2$, we obtain

$$(2.6) \quad \int_{\partial\Omega_{\text{int}}} -2\theta \frac{d\phi}{dx} \geq \int_{\partial\Omega_{\text{int}}} -\frac{1}{\sigma} \theta^2 - \sigma \left(\frac{d\phi}{dx} \right)^2.$$

From the trace theorem [22], and recalling that θ is zero on some part Σ of $\partial\Omega$ to invoke Poincaré–Friedrichs, there exists a constant $\bar{\rho}(\Omega) > 0$ such that

$$\int_{\partial\Omega} \theta^2 \leq \bar{\rho}(\Omega) \int_{\Omega} |\nabla \theta|^2$$

(we henceforth suppress the dependence of $\bar{\rho}$ on Ω). We now choose $\sigma = \frac{\mathcal{F}}{\text{Bi}_{\text{int}}}$ in (2.6) and invoke the trace result to obtain

$$(2.7) \quad -\tau \text{Bi}_{\text{int}} \int_{\partial\Omega_{\text{int}}} \theta \frac{d\phi}{dx} \geq -\frac{1}{2} \tau \frac{\bar{\rho} \text{Bi}_{\text{int}}^2}{\mathcal{F}} \int_{\Omega} |\nabla \theta|^2 - \frac{1}{2} \tau \mathcal{F} \int_{\partial\Omega_{\text{int}}} \left(\frac{d\phi}{dx} \right)^2.$$

So, finally, noting that $\text{Bi}_{\text{int}} \int_{\partial\Omega_{\text{int}}} (\theta - \phi)^2 > 0$ and applying (2.7), we find

$$(2.8) \quad \begin{aligned} a(w, w^*) &\geq \left(1 - \frac{1}{2} \tau \frac{\bar{\rho} \text{Bi}_{\text{int}}^2}{\mathcal{F}} \right) \int_{\Omega} |\nabla \theta|^2 + \frac{1}{2} \tau \mathcal{F} \int_{\partial\Omega_{\text{int}}} \left(\frac{d\phi}{dx} \right)^2 + \frac{1}{2} (\mathcal{F} + \tau \text{Bi}_{\text{int}}) \phi^2(\Lambda) \\ &\geq K(\tau) \|w\|_X^2 \end{aligned}$$

for τ small enough and

$$K(\tau) = \min \left(1 - \frac{1}{2}\tau \frac{\bar{\rho}\text{Bi}_{\text{int}}^2}{\mathcal{F}}, \frac{1}{2}\tau\mathcal{F}, \frac{1}{2}(\mathcal{F} + \tau\text{Bi}_{\text{int}}) \right).$$

Also, from the Cauchy–Schwarz inequality, we have

$$\int_{[0,\Lambda]} \phi(y)^2 dy \leq \int_{[0,\Lambda]} \left(\int_{[0,y]} \frac{d\phi}{dx}(x) dx \right)^2 dy \leq \Lambda^2 \int_{[0,\Lambda]} \frac{d\phi^2}{dx}(x) dx \quad \forall \phi \in V,$$

and as a consequence

$$\int_{[0,\Lambda]} \left(\phi + \tau \frac{d\phi}{dx} \right)^2 \leq \int_{[0,\Lambda]} 2 \left(\phi^2 + \tau^2 \left(\frac{d\phi}{dx} \right)^2 \right) \leq 2(\Lambda^2 + \tau^2) \int_{[0,\Lambda]} \left(\frac{d\phi}{dx} \right)^2.$$

Defining

$$(2.9) \quad C(\tau) = \max \left(1, \sqrt{2(\Lambda^2 + \tau^2)} \right),$$

it follows that

$$(2.10) \quad \|w^*\|_Z \leq C(\tau)\|w\|_X \quad \forall w \in X.$$

This proves the inf-sup stability of $a(\cdot, \cdot)$:

$$\inf_{w \in X} \sup_{v \in Z} \frac{a(w, v)}{\|w\|_X \|v\|_Z} \geq \inf_{w \in X} \frac{a(w, w^*)}{\|w\|_X \|w^*\|_Z} \geq \inf_{w \in X} \frac{K(\tau)\|w\|_X}{\|w^*\|_Z} \geq \frac{K(\tau)}{C(\tau)} > 0,$$

and hence $\beta_0(\tau) \equiv \frac{K(\tau)}{C(\tau)}$ is a lower bound for the inf-sup constant.

The continuity of $a(\cdot, \cdot)$ as defined in (2.3) follows from the trace theorem and the Cauchy–Schwarz inequality: for example

$$\begin{aligned} \left| \int_{\Omega} \nabla \theta \nabla \vartheta \right| &\leq \left(\int_{\Omega} |\nabla \theta|^2 \right)^{\frac{1}{2}} \left(\int_{\Omega} |\nabla \vartheta|^2 \right)^{\frac{1}{2}} \leq \|w\|_X \|v\|_Z, \\ \left| \int_{\partial\Omega_{\text{int}}} \theta \vartheta \right| &\leq \left(\int_{\partial\Omega_{\text{int}}} \theta^2 \right)^{\frac{1}{2}} \left(\int_{\partial\Omega_{\text{int}}} \vartheta^2 \right)^{\frac{1}{2}} \\ &\leq \bar{\rho}^2 \left(\int_{\Omega} |\nabla \theta|^2 \right)^{\frac{1}{2}} \left(\int_{\Omega} |\nabla \vartheta|^2 \right)^{\frac{1}{2}} \leq \bar{\rho}^2 \|w\|_X \|v\|_Z, \\ \left| \int_{\partial\Omega_{\text{int}}} \phi \varphi \right| &\leq \left(\int_{\partial\Omega_{\text{int}}} \phi^2 \right)^{\frac{1}{2}} \left(\int_{\partial\Omega_{\text{int}}} \varphi^2 \right)^{\frac{1}{2}} \\ &\leq \Lambda \left(\int_{[0,\Lambda]} \frac{d\phi^2}{dx} \right)^{\frac{1}{2}} \left(\int_{[0,\Lambda]} \varphi^2 \right)^{\frac{1}{2}} \leq \Lambda \|w\|_X \|v\|_Z. \end{aligned}$$

Applying the same ideas to all the terms in $a(w, v)$, we obtain

$$|a(w, v)| \leq \gamma_0 \|w\|_X \|v\|_Z \quad \forall w \in X; v \in Z,$$

where γ_0 is an upper bound for the continuity constant defined as

$$\gamma_0 \equiv 1 + \text{Bi}_{\text{ext}}\bar{\rho}^2 + \text{Bi}_{\text{int}}\bar{\rho}^2 + \Lambda\text{Bi}_{\text{int}}\bar{\rho} + \text{Bi}_{\text{int}}\bar{\rho} + \Lambda\text{Bi}_{\text{int}} + \mathcal{F}. \quad \square$$

It can also be shown that $(a(w, v) = 0 \forall w \in X) \Rightarrow (v = 0)$ which, in conjunction with Lemma 2.1, proves the well-posedness of (2.5) from the Banach–Nečas–Babuška theorem [6]. Note that our assumption of Dirichlet conditions on Σ can be relaxed such that we consider what we shall denote the “all natural” problem in which $Y = H^1(\Omega)$. In this case we invoke the complete H^1 norm over Ω to retain well-posedness. Throughout this paper (for convenience of exposition and simplicity), the rigorous analysis will be applied to Y as defined above (i.e., with homogeneous Dirichlet conditions over part of $\partial\Omega$); however, for purposes of interpretation, we shall on occasion consider the “all natural” problem.

2.3. Finite element discretization. Let \mathcal{T}_h be a simplicial mesh of Ω and let \mathcal{S}_h be a mesh of $[0, \Lambda]$. We assume that the restriction of \mathcal{T}_h to the top or bottom part of $\partial\Omega_{\text{int}}$ is equal to \mathcal{S}_h . We introduce the following discrete spaces: $Y_h \subset Y$, the \mathbb{P}_1 finite element space associated with \mathcal{T}_h ; $V_h \subset V$, the \mathbb{P}_1 finite element space associated with \mathcal{S}_h ; $W_h \subset W$, the \mathbb{P}_0 finite element space associated with \mathcal{S}_h ; $X_h = Y_h \times V_h$; and $Z_h = Y_h \times W_h$. Note that the dimensions of V_h and W_h are the same thanks to the condition $\phi(0) = 0$. Also, for $\phi_h \in V_h$, we denote by $\bar{\phi}_h \in W_h$ the average of ϕ_h over each element in \mathcal{S}_h . We now invoke these spaces to provide a Petrov–Galerkin approximation of (2.3).

We define the bilinear form $a_h(\cdot, \cdot)$ on $X_h \times Z_h$ such that for $w_h \in X_h$ and $v_h \in Z_h$,

$$(2.11) \quad \begin{aligned} a_h(u_h, v_h) = & \int_{\Omega} \nabla \theta_h \nabla \vartheta_h + \text{Bi}_{\text{ext}} \int_{\partial\Omega_{\text{ext}}} \theta_h \vartheta_h \\ & + \text{Bi}_{\text{int}} \int_{\partial\Omega_{\text{int}}} (\theta_h - \bar{\phi}_h) \vartheta_h - \text{Bi}_{\text{int}} \int_{\partial\Omega_{\text{int}}} (\theta_h - \bar{\phi}_h) \varphi_h + \mathcal{F} \int_{[0, \Lambda]} \frac{d\phi_h}{dx} \varphi_h. \end{aligned}$$

Note that $a_h(w_h, v_h)$ differs from $a(w_h, v_h)$ due to the $\bar{\phi}_h$ terms. The problem for the discrete solution u_h can then be stated: find $u_h \in X_h$ such that

$$(2.12) \quad a_h(u_h, v_h) = f(v_h) \quad \forall v_h \in Z_h.$$

LEMMA 2.2. *The bilinear form $a_h(\cdot, \cdot)$ is inf-sup stable and continuous on $X_h \times Z_h$.*

Proof. The proof is very similar to the continuous case, except that the definition of w_h^* is slightly different. For any $w_h = (\theta_h, \phi_h) \in X_h$, we define $w_h^* = (\theta_h, \bar{\phi}_h + \tau \frac{d\phi_h}{dx}) \in Z_h$ for a small real positive constant τ : we must take the average of ϕ_h to remain in the required discrete test space. Then, exactly as before, we arrive at

$$(2.13) \quad \begin{aligned} a_h(w_h, w_h^*) & \geq \left(1 - \frac{1}{2}\tau \frac{\rho \text{Bi}_{\text{int}}^2}{\mathcal{F}}\right) \int_{\Omega} |\nabla \theta_h|^2 + \frac{1}{2}\tau \mathcal{F} \int_{\partial\Omega_{\text{int}}} \left(\frac{d\phi_h}{dx}\right)^2 + \frac{1}{2}(\mathcal{F} + \tau \text{Bi}_{\text{int}}) \phi_h^2(\Lambda) \\ & \geq K(\tau) \|u_h\|_X^2. \end{aligned}$$

The key observations are that the $\bar{\phi}_h$ in $a_h(\cdot, \cdot)$ and w_h^* “match” and that $\int_{[0, \Lambda]} \bar{\phi}_h \frac{d\phi_h}{dx} = \int_{[0, \Lambda]} \phi_h \frac{d\phi_h}{dx}$. Also, on each element, we have

$$\int_0^h \left(\frac{1}{h} \int_0^h \phi_h\right)^2 \leq \frac{1}{h^2} \int_0^h \left(\int_0^h \phi_h\right)^2 \leq \frac{1}{h^2} \int_0^h h \left(\int_0^h \phi_h^2\right) \leq \int_0^h \phi_h^2,$$

and so we obtain

$$(2.14) \quad \int_{[0, \Lambda]} \bar{\phi}_h^2 \leq \int_{[0, \Lambda]} \phi_h^2 \quad \forall \phi_h \in V_h;$$

as a consequence, we retain

$$(2.15) \quad \|w_h^*\|_Z \leq C(\tau)\|w_h\|_X \quad \forall w_h \in X_h.$$

This proves the inf-sup stability of $a_h(\cdot, \cdot)$:

$$(2.16) \quad \inf_{w_h \in X_h} \sup_{v_h \in Z_h} \frac{a_h(w_h, v_h)}{\|w_h\|_X \|v_h\|_Z} \geq \inf_{w_h \in X_h} \frac{a_h(w_h, w_h^*)}{\|w_h\|_X \|w_h^*\|_Z} \geq \frac{K(\tau)}{C(\tau)} > 0.$$

The continuity proof for $a_h(\cdot, \cdot)$ is the same as for $a(\cdot, \cdot)$ once we appeal to (2.14). \square

We thus note that $\beta_0(\tau) \equiv \frac{K(\tau)}{C(\tau)}$, introduced earlier, is also a lower bound for the inf-sup constant of $a_h(\cdot, \cdot)$. We now provide details for the computation of this quantity which shall be needed later for RB a posteriori error estimation. We choose $\tau = \hat{\tau}$ such that

$$(2.17) \quad 1 - \frac{1}{2} \hat{\tau} \frac{\bar{\rho} \text{Bi}_{\text{int}}^2}{\mathcal{F}} = \frac{1}{2} \hat{\tau} \mathcal{F} \iff \hat{\tau} = \frac{2}{\mathcal{F} + \frac{\bar{\rho} \text{Bi}_{\text{int}}^2}{\mathcal{F}}}$$

and for which

$$(2.18) \quad K(\hat{\tau}) = \frac{1}{2} \hat{\tau} \mathcal{F};$$

and $C(\hat{\tau}) = \sqrt{2(\Lambda^2 + \hat{\tau}^2)}$ from (2.9) and our standard assumptions $\mathcal{F} \geq 2$, $\hat{\tau} \leq 1$ and $\Lambda > 1$. Thus for an inf-sup lower bound, we may choose

$$(2.19) \quad \beta_0^{\text{LB}}(\hat{\tau}) \equiv \frac{\hat{\tau} \mathcal{F}}{2\sqrt{2(\Lambda^2 + \hat{\tau}^2)}}$$

for $\hat{\tau}$ given by (2.17).

LEMMA 2.3. *Let u and u_h be the solutions to the continuous and discrete problems, respectively, and let h be the mesh size. Assuming that $u \in X \cap H^2(\Omega) \times H^2([0, \Lambda])$, we then have the following a priori error estimate:*

$$\|u - u_h\|_X \leq \mathcal{O}(h)(\|u\|_X + |u|_2),$$

where $|\cdot|_2$ is the Sobolev seminorm on $H^2(\Omega) \times H^2([0, \Lambda])$.

Proof. The proof is standard and invokes the first Strang lemma to arrive at

$$\beta_0 \|u_h - w_h\|_X \leq \gamma_0 \|u - w_h\|_X + \sup_{v_h \in Z_h} \frac{|a(w_h, v_h) - a_h(w_h, v_h)|}{\|v_h\|_Z}.$$

Let ϕ_h be the component in V_h of w_h . Then from (2.3) and (2.11) it follows that

$$a(w_h, v_h) - a_h(w_h, v_h) = \text{Bi}_{\text{int}} \int_{\partial\Omega_{\text{int}}} (\phi_h - \bar{\phi}_h)(\varphi_h - \vartheta_h),$$

and it is then straightforward to show that

$$\sup_{v_h \in Z_h} \frac{|a(w_h, v_h) - a_h(w_h, v_h)|}{\|v_h\|_Z} \leq Mh(\|u - w_h\|_X + \|u\|_X)$$

for M independent of h . We thus obtain

$$\|u_h - w_h\|_X \leq \frac{\gamma_0 + Mh}{\beta_0} \|u - w_h\|_X + \frac{M}{\beta_0} h \|u\|_X.$$

The desired a priori estimate then follows from standard results in approximation theory [22] and the triangle inequality. \square

3. Reduced basis approximation.

3.1. RB spaces. In the following, we now consider the dependence on the parameter $\boldsymbol{\mu} = (\text{Bi}_{\text{ext}}, \text{Bi}_{\text{int}}, \mathcal{F})$, which belongs to a parameter domain $D \subset \mathbb{R}^3$. The FE weak form reads, with explicit parameter dependence now indicated: find $u_h(\boldsymbol{\mu}) \in X_h$ such that $a_h(u_h(\boldsymbol{\mu}), v_h; \boldsymbol{\mu}) = f(v_h) \forall v_h \in Z_h$.

We first form the RB *trial spaces* $X_N \subset X_h$, $1 \leq N \leq N_{\text{max}}$. We introduce the set of parameters

$$(3.1) \quad S_N = \{\boldsymbol{\mu}^1, \dots, \boldsymbol{\mu}^N\}, \quad 1 \leq N \leq N_{\text{max}},$$

as provided by a greedy algorithm [20], and then define the nested spaces

$$(3.2) \quad X_N = \text{span}\{u_h(\boldsymbol{\mu}^n), \quad 1 \leq n \leq N\}, \quad 1 \leq N \leq N_{\text{max}}.$$

The $u_h(\boldsymbol{\mu}^n)$, $1 \leq n \leq N_{\text{max}}$, are often referred to as “snapshots” of the parametric manifold $\mathcal{M}_h = \{u_h(\boldsymbol{\mu}) | \boldsymbol{\mu} \in D\}$. It is clear that if, indeed, the manifold is low-dimensional and smooth, then we would expect to well approximate any member of the manifold—any solution $u_h(\boldsymbol{\mu})$ for some $\boldsymbol{\mu}$ in \mathcal{D} —in terms of relatively few snapshots.

In order to understand the RB *test spaces* we return to the inf-sup discussion of section 2.3. In particular, we recall that we defined the quantity $\hat{\tau}$ in (2.17) as a function of the parameters $\boldsymbol{\mu}$. Now that we consider RB approximations, the parameters are allowed to vary and so we introduce

$$\hat{\tau}_{\min} = \frac{2}{\mathcal{F}_{\max} + \frac{\bar{\rho} \text{Bi}_{\text{int,max}}^2}{\mathcal{F}_{\min}}},$$

where $\mathcal{F} \in [\mathcal{F}_{\min}, \mathcal{F}_{\max}]$, $\text{Bi}_{\text{int,max}}$ is the maximum of Bi_{int} in D , and $\bar{\rho}$ is the trace constant computed by solving an eigenproblem. Hence $\hat{\tau}_{\min}$ is independent of $\boldsymbol{\mu}$ and the choice $\hat{\tau} = \hat{\tau}_{\min}$ ensures that (2.19) remains valid for all $\boldsymbol{\mu} \in D$; note that $\beta_0^{LB}(\hat{\tau})$ is an increasing function of $\hat{\tau}$. We also define the * superscript in what follows as

$$(3.3) \quad u_h^* = \left(\theta_h, \bar{\phi}_h + \hat{\tau}_{\min} \frac{d\phi_h}{dx} \right) \in Z_h$$

for any $u_h = (\theta_h, \phi_h) \in X_h$. We are now ready to properly define the RB test space as $Z_N = \{w_N^* | w_N \in X_N\} \subset Z_h$. We can now directly define our RB approximation: find $u_N(\boldsymbol{\mu}) \in X_N$ such that

$$(3.4) \quad a_h(u_N(\boldsymbol{\mu}), v_N; \boldsymbol{\mu}) = f(v_N) \quad \forall v_N \in Z_N.$$

The well-posedness of this discrete problem follows from the inf-sup discussion provided above.

We define the parameter independent quantities

$$\bar{\beta}_0^{LB} = \frac{\hat{\tau}_{\min} \mathcal{F}_{\min}}{2\sqrt{2(\Lambda^2 + \hat{\tau}_{\min}^2)}},$$

$$\bar{\gamma}_0^{UB} \equiv 1 + \text{Bi}_{\text{ext,max}} \bar{\rho}^2 + \text{Bi}_{\text{int,max}} \bar{\rho}^2 + \Lambda \text{Bi}_{\text{int,max}} \bar{\rho} + \text{Bi}_{\text{int,max}} \bar{\rho} + \Lambda \text{Bi}_{\text{int,max}} + \mathcal{F}_{\max},$$

which correspond to a parameter independent lower bound for the inf-sup stability constant and to a parameter independent upper bound for the continuity constant, respectively, among all possible parameter values.

PROPOSITION 3.1. *We have the following a priori error result for the RB approximation:*

$$\|u_h(\boldsymbol{\mu}) - u_N(\boldsymbol{\mu})\|_X \leq \left(1 + \frac{\overline{\gamma}_0^{UB}}{\underline{\beta}_0^{LB}}\right) \inf_{w_N \in X_N} \|u_h(\boldsymbol{\mu}) - w_N\|_X.$$

We refer to [24] for a proof of this result. Note that in our case, thanks to (3.3), the supremizer operator is effectively parameter independent.

This demonstrates that the quality of our RB solution depends entirely on the approximation properties of our RB spaces. Under certain assumptions [3, 2], it can be shown that the RB greedy spaces yield convergence rates similar to the optimal Kolmogorov N -width.

3.2. A posteriori error estimation. The central equation in a posteriori theory is the error residual relationship. The error $e(\boldsymbol{\mu}) \equiv u_h(\boldsymbol{\mu}) - u_N(\boldsymbol{\mu}) \in X_h$ satisfies $a_h(e(\boldsymbol{\mu}), v; \boldsymbol{\mu}) = r(v; \boldsymbol{\mu}) \forall v \in Z_h$, where $r(v; \boldsymbol{\mu}) \in Z'_h$ (the dual space of Z_h) is the residual, $r(v; \boldsymbol{\mu}) \equiv f(v; \boldsymbol{\mu}) - a_h(u_N(\boldsymbol{\mu}), v; \boldsymbol{\mu}) \forall v \in Z_h$. It is clear that r is bounded since f and a_h are bounded. We define the error estimator $\Delta_N(\boldsymbol{\mu}) \equiv \frac{\|r(\cdot; \boldsymbol{\mu})\|_{Z'_h}}{\beta_0(\boldsymbol{\mu})}$, for which we can prove [25] $\|u_h(\boldsymbol{\mu}) - u_N(\boldsymbol{\mu})\|_X \leq \Delta_N(\boldsymbol{\mu})$. We will take advantage of this error bound in the standard Greedy algorithm [20] to construct the RB spaces of section 3.1, and also to certify the RB predictions. We note that rather than $\beta_0^{LB}(\hat{r}_{\min})$, a sharper lower bound may be obtained by the successive constraint method [14].

3.3. Offline-online strategy. We now consider the discrete equations associated with the Petrov–Galerkin approximation (3.4). We must first choose an appropriate basis for our spaces. To this end, we apply the Gram–Schmidt process in the $(\cdot, \cdot)_X$ inner product to our snapshots $u_h(\boldsymbol{\mu}^n)$, $1 \leq n \leq N_{\max}$, to obtain mutually orthonormal functions ζ_n , $1 \leq n \leq N_{\max}$: $(\zeta_n, \zeta_m)_X = \delta_{nm}$, $1 \leq n, m \leq N_{\max}$, where δ_{nm} is the Kronecker-delta symbol. We then choose the sets $\{\zeta_n\}_{n=1, \dots, N}$ as our bases for X_N , $1 \leq N \leq N_{\max}$. We now insert

$$(3.5) \quad u_N(\boldsymbol{\mu}) = \sum_{m=1}^N u_{Nm}(\boldsymbol{\mu}) \zeta_m,$$

and $v_N = \zeta_n^*$, $1 \leq n \leq N$, into (3.4) to obtain the RB “stiffness” equations

$$(3.6) \quad \sum_{m=1}^N a_h(\zeta_m, \zeta_n^*; \boldsymbol{\mu}) u_{Nm}(\boldsymbol{\mu}) = f(\zeta_n^*), \quad 1 \leq n \leq N,$$

for the RB coefficients $u_{Nm}(\boldsymbol{\mu})$, $1 \leq m \leq N$. The offline-online strategy is standard and it thus suffices to excerpt a brief description from [23]. We note that our system (3.6) can be expressed, thanks to (2.4), as

$$(3.7) \quad \sum_{m=1}^N \left(\sum_{q=1}^Q \Theta^q(\boldsymbol{\mu}) a^q(\zeta_m, \zeta_n^*) \right) u_{Nm}(\boldsymbol{\mu}) = f(\zeta_n), \quad 1 \leq n \leq N.$$

In the offline stage, we first compute the $u_h(\boldsymbol{\mu}^n)$, $1 \leq n \leq N_{\max}$, and subsequently the ζ_n , $1 \leq n \leq N_{\max}$; we then form and store the $f(\zeta_n)$, $1 \leq n \leq N_{\max}$, and

$$(3.8) \quad a^q(\zeta_m, \zeta_n^*), \quad 1 \leq n, m \leq N_{\max}, \quad 1 \leq q \leq Q.$$

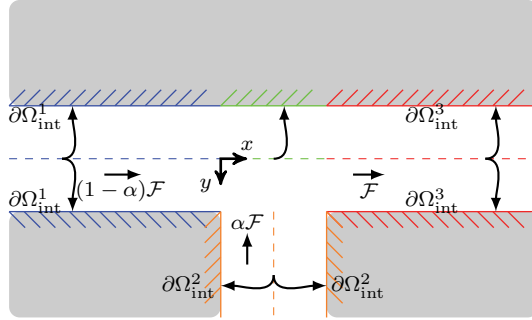


FIG. 2. A channel mixing component: the colors indicate the identity mappings from $\partial\Omega$ to the fluid mixed-mean temperature filament coordinate.

The offline operation count depends on N_{\max} , Q , and \mathcal{N} . In the online (or “deployed”) stage, we retrieve (3.8) to form

$$(3.9) \quad \sum_{q=1}^Q \Theta^q(\boldsymbol{\mu}) a^q(\zeta_m, \zeta_n^*), \quad 1 \leq n, m \leq N,$$

and we solve the resulting $N \times N$ stiffness system (3.7) to obtain the $u_{Nm}(\boldsymbol{\mu})$, $1 \leq m \leq N$.

The online operation count is $O(QN^2)$ to perform the sum (3.9) and $O(N^3)$ to invert (3.7)—note that the RB stiffness matrix is full. The online cost—and hence marginal cost and also asymptotic average cost—to evaluate $\boldsymbol{\mu} \rightarrow u_N(\boldsymbol{\mu})$ is thus independent of \mathcal{N} . The implications are two-fold: first, if N is indeed small, we will achieve very fast response in real-time and many-query contexts; second, we may choose \mathcal{N} very conservatively—to effectively eliminate the error between the exact and FE predictions—without adversely affecting the online (marginal) cost. A similar but more involved offline-online strategy may be developed for the error bound; we refer the reader to [23].

4. More advanced models.

4.1. Channel mixing. We consider here the case in which two fluid channels mix into a single channel, as shown in Figure 2. The flows $\alpha\mathcal{F}$ and $(1 - \alpha)\mathcal{F}$ are merging into \mathcal{F} , where $\alpha \in [0.1, 0.9]$ is an additional “flow distribution” parameter.

We describe the main additions to the theory presented in section 2.2. First, we define three different variables for the fluid bulk temperature, corresponding to the two incoming channels plus the mixing channel: ϕ_1 is defined on $[0, \Lambda_1]$, where Λ_1 is the nondimensional length of the incoming horizontal channel (blue and left half of green); ϕ_2 is defined on $[0, \Lambda_2]$, where Λ_2 is the nondimensional length of the vertical channel (orange); and ϕ_3 is defined on $[0, \Lambda_3]$, where Λ_3 is the nondimensional length of the mixing horizontal channel (right half of green and red). The mapping of the fluid 1D domain to the channel walls is less trivial in this case; the different types of mapping are represented by colors in Figure 2.

We change the definition of the fluid spaces V and W to

$$\begin{aligned} V &= \{(\phi_1, \phi_2, \phi_3) \mid \phi_1 \in H^1([0, \Lambda_1]), \phi_1(0) = 0, \phi_2 \in H^1([0, \Lambda_2]), \phi_2(0) = 0, \\ &\quad \phi_3 \in H^1([0, \Lambda_3]), \phi_3(0) = (1 - \alpha)\phi_1(\Lambda_1) + \alpha\phi_2(\Lambda_2)\}; \\ W &= L^2([0, \Lambda_1]) \times L^2([0, \Lambda_2]) \times L^2([0, \Lambda_3]). \end{aligned}$$

We also introduce the notation $u = (\theta, \phi_1, \phi_2, \phi_3) \in X = Y \times V$, $v = (\vartheta, \varphi_1, \varphi_2, \varphi_3) \in Z = Y \times W$, and we define the following norms on X and Z :

$$\begin{aligned} \|u\|_X^2 &= \int_{\Omega} |\nabla\theta|^2 + \int_{[0,\Lambda_1]} \left(\frac{d\phi_1}{dx}\right)^2 + \int_{[0,\Lambda_2]} \left(\frac{d\phi_2}{dy}\right)^2 + \int_{[0,\Lambda_3]} \left(\frac{d\phi_3}{dy}\right)^2 + \phi_3^2(\Lambda_3), \\ \|v\|_Z^2 &= \int_{\Omega} |\nabla\vartheta|^2 + \int_{[0,\Lambda_1]} \varphi_1^2 + \int_{[0,\Lambda_2]} \varphi_2^2 + \int_{[0,\Lambda_3]} \varphi_3^2. \end{aligned}$$

The bilinear form $a(\cdot, \cdot)$ now reads

$$\begin{aligned} a(w, v) &= \int_{\Omega} \nabla\theta\nabla\vartheta + \text{Bi}_{\text{ext}} \int_{\partial\Omega_{\text{ext}}} \theta\vartheta \\ &\quad + \text{Bi}_{\text{int}} \int_{\partial\Omega_{\text{int}}^1} (\theta - \phi_1)\vartheta + \text{Bi}_{\text{int}} \int_{\partial\Omega_{\text{int}}^2} (\theta - \phi_2)\vartheta + \text{Bi}_{\text{int}} \int_{\partial\Omega_{\text{int}}^3} (\theta - \phi_3)\vartheta \\ &\quad - \text{Bi}_{\text{int}} \int_{\partial\Omega_{\text{int}}^1} (\theta - \phi_1)\varphi_1 + (1 - \alpha)\mathcal{F} \int_{[0,\Lambda_1]} \frac{d\phi_1}{dx} \varphi_1 \\ &\quad - \text{Bi}_{\text{int}} \int_{\partial\Omega_{\text{int}}^2} (\theta - \phi_2)\varphi_2 + \alpha\mathcal{F} \int_{[0,\Lambda_2]} \frac{d\phi_2}{dy} \varphi_2 \\ (4.1) \quad &\quad - \text{Bi}_{\text{int}} \int_{\partial\Omega_{\text{int}}^3} (\theta - \phi_3)\varphi_3 + \mathcal{F} \int_{[0,\Lambda_3]} \frac{d\phi_3}{dy} \varphi_3. \end{aligned}$$

The weak form is then as follows: find $u \in X$ such that $a(u, v) = f(v) \forall v \in Z$.

This channel mixing model preserves thermal energy. For simplicity we consider the “all-natural” situation, in which case we may choose for our test function $\chi = 1$. Then the heat source in the system corresponds to $f(\chi)$, and we obtain

$$\begin{aligned} (4.2) \quad f(\chi) &= a(u, \chi) \\ &= \text{Bi}_{\text{ext}} \int_{\partial\Omega_{\text{ext}}} \theta + (1 - \alpha)\mathcal{F} \int_{[0,\Lambda_1]} \frac{d\phi_1}{dx} + \alpha\mathcal{F} \int_{[0,\Lambda_2]} \frac{d\phi_2}{dx} + \mathcal{F} \int_{[0,\Lambda_3]} \frac{d\phi_3}{dy} \\ &= \text{Bi}_{\text{ext}} \int_{\partial\Omega_{\text{ext}}} \theta + (1 - \alpha)\mathcal{F}\phi_1(\Lambda_1) + \alpha\mathcal{F}\phi_2(\Lambda_2) + \mathcal{F}(\phi_3(\Lambda_3) - \phi_3(0)) \\ &= \text{Bi}_{\text{ext}} \int_{\partial\Omega_{\text{ext}}} \theta + \mathcal{F}\phi_3(\Lambda_3). \end{aligned}$$

This corresponds to a global heat balance: heat generated leaves through the wall or with the fluid.

LEMMA 4.1. *The bilinear form $a(\cdot, \cdot)$ is inf-sup stable.*

Proof. As in section 2.2, we consider $a(w, w^*)$, but the following new boundary terms appear due to the channel mixing:

$$\begin{aligned} &(1 - \alpha)\mathcal{F} \int_{[0,\Lambda_1]} \frac{d\phi_1}{dx} \phi_1 + \alpha\mathcal{F} \int_{[0,\Lambda_2]} \frac{d\phi_2}{dy} \phi_2 + \mathcal{F} \int_{[0,\Lambda_3]} \frac{d\phi_3}{dx} \phi_3 \\ &= (1 - \alpha)\mathcal{F}\phi_1^2(\Lambda_1) + \alpha\mathcal{F}\phi_2^2(\Lambda_2) + \mathcal{F}(\phi_3^2(\Lambda_3) - \phi_3^2(0)) \\ (4.3) \quad &= \alpha(1 - \alpha)\mathcal{F}(\phi_1(\Lambda_1) - \phi_2(\Lambda_2))^2 + \mathcal{F}\phi_3^2(\Lambda_3), \end{aligned}$$

where we used the equality $\phi_3(0) = (1 - \alpha)\phi_1(\Lambda_1) + \alpha\phi_2(\Lambda_2)$. The term $\mathcal{F}\phi_3^2(\Lambda_3)$ is directly related to the X -norm. The remaining term $\alpha(1 - \alpha)\mathcal{F}(\phi_1(\Lambda_1) - \phi_2(\Lambda_2))^2$

is positive, and hence can be neglected in the stability proof. The rest of the proof follows exactly the same arguments as in section 2.2. \square

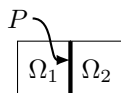
The rest of the theory (FE, RB) is similar to the straight-channel case. Note that for this mixing case, the mathematical model is clearly very approximate. We will not be able to easily characterize the complexity of the mixing with a constant heat transfer coefficient. However, it corresponds to a physical limit for which we assume very good mixing. The same comment also applies to the splitting case described below.

4.2. Channel splitting. The channel splitting situation is very similar to the channel mixing, and corresponds to Figure 2 with the flow directions reversed. The main difference compared with the mixing case is the continuity condition at the point where the flow splits/mixes: in the mixing case, the fluid mixed-mean temperature after mixing is a weighted average of the two incoming fluid temperatures, with weights α and $(1 - \alpha)$; in the splitting case, we simply enforce continuity of the fluid mixed-mean temperature. The respective conditions ensure the thermal energy conservation of the model while retaining the stability of the bilinear form.

5. Systemization. We now consider the models presented in the previous sections as components (or subdomains) from which we will build a system composed of many similar components connected at ports. To this end, we will apply a static condensation reduced basis element method, which is a domain synthesis approach with the following distinct features: reduced basis approximation of finite element bubble functions at the intradomain level; eigenfunction “port” representation at the interface level; static condensation at the interdomain level.

The general methodology of scRBE is described in [12] in a rigorous and abstract framework. Here we use a different path and we present the method based on a simple example with two subdomains, focusing on matrix transformations of the linear system derived from the PDE FE discretization. We aim to provide a complementary view of scRBE with emphasis on the extensions required for the fluid convection equation.

5.1. Static condensation. We suppose our system domain Ω is composed of two components, Ω_1 and Ω_2 , which share a part of their boundary, P , denoted a port, as described by the next simple figure.



The PDE finite element approximation yields the global system

$$\begin{bmatrix} A_P & A_{P,\Omega_1}^T & A_{P,\Omega_2}^T \\ A_{P,\Omega_1} & A_{\Omega_1} & 0 \\ A_{P,\Omega_2} & 0 & A_{\Omega_2} \end{bmatrix} \begin{bmatrix} \mathbf{u}_P \\ \mathbf{u}_{\Omega_1} \\ \mathbf{u}_{\Omega_2} \end{bmatrix} = \begin{bmatrix} \mathbf{f}_P \\ \mathbf{f}_{\Omega_1} \\ \mathbf{f}_{\Omega_2} \end{bmatrix},$$

where we group and reorder to segregate the degrees of freedom on P from the degrees of freedom internal to Ω_1 and Ω_2 .

We now apply static condensation to remove the degrees of freedom internal to each component. We define the Schur complement matrix A_{SC} and the Schur right-

hand side \mathbf{f}_{SC} as

$$(5.1) \quad A_{\text{SC}} = A_{\text{P}} - A_{\text{P},\Omega_1}^{\text{T}} A_{\Omega_1}^{-1} A_{\text{P},\Omega_1} - A_{\text{P},\Omega_2}^{\text{T}} A_{\Omega_2}^{-1} A_{\text{P},\Omega_2},$$

$$(5.2) \quad \mathbf{f}_{\text{SC}} = \mathbf{f}_{\text{P}} - A_{\text{P},\Omega_1}^{\text{T}} A_{\Omega_1}^{-1} \mathbf{f}_{\Omega_1} - A_{\text{P},\Omega_2}^{\text{T}} A_{\Omega_2}^{-1} \mathbf{f}_{\Omega_2}.$$

The vector of port coefficients \mathbf{u}_{P} is then the solution of the Schur complement system

$$A_{\text{SC}} \mathbf{u}_{\text{P}} = \mathbf{f}_{\text{SC}},$$

which is of size \mathcal{N}_{P} , the number of degrees of freedom on P . We observe that computation of the quantity $A_{\Omega_i}^{-1} A_{\text{P},\Omega_i}$ corresponds to computation of \mathcal{N}_{P} FE solutions of a PDE defined over Ω_i with homogeneous Dirichlet conditions on P and different source terms (arising from the lifting of the port degrees of freedom). We denote by “FE bubbles” the solutions to these PDEs, one solution associated to each degree of freedom on P ; we introduce \mathbf{b}_k^i as the vector of FE coefficients for the bubble in Ω_i associated to the k th degree of freedom on P . Hence we can write

$$A_{\Omega_i}^{-1} A_{\text{P},\Omega_i} = A_{\Omega_i}^{-1} [\mathbf{a}_1^i \mathbf{a}_2^i \cdots \mathbf{a}_{\mathcal{N}_{\text{P}}}^i] = \underbrace{[\mathbf{b}_1^i \mathbf{b}_2^i \cdots \mathbf{b}_{\mathcal{N}_{\text{P}}}^i]}_{\mathcal{N}_i \times \mathcal{N}_{\text{P}}},$$

where \mathbf{a}_k^i is the source term (lifted port degree of freedom) for the k th bubble and \mathcal{N}_i is the number of degrees of freedom internal to Ω_i .

5.2. Static condensation with reduced basis. We now replace the FE bubbles by RB bubble approximations (with an RB space of dimension N):

$$\mathbf{b}_k^i \longrightarrow B_k^i \tilde{\mathbf{b}}_k^i,$$

where B_k^i is the matrix of size $\mathcal{N}_i \times N$ of FE coefficients of the RB basis functions (the ζ_n , $1 \leq n \leq N$), and $\tilde{\mathbf{b}}_k^i$ are the coefficients of the bubble in the RB space of dimension N (3.5). We can see that the matrix B_k^i is different for each i, k : we construct a *different* RB space for each bubble. The RB bubble coefficients $\tilde{\mathbf{b}}_k^i$ are obtained by solution of a linear system of size $N \times N$ $\tilde{\mathbf{b}}_k^i = \tilde{A}_{\Omega_i,k}^{-1} \tilde{\mathbf{a}}_k^i$, where $\tilde{A}_{\Omega_i,k}$ and $\tilde{\mathbf{a}}_k^i$ are given (effectively) by (3.6). Hence in the end we effect the following substitution:

$$A_{\Omega_i}^{-1} A_{\text{P},\Omega_i} \longrightarrow \left[B_1^i \tilde{A}_{\Omega_i,1}^{-1} \tilde{\mathbf{a}}_1^i \quad B_2^i \tilde{A}_{\Omega_i,2}^{-1} \tilde{\mathbf{a}}_2^i \quad \cdots \quad B_{\mathcal{N}_{\text{P}}}^i \tilde{A}_{\Omega_i,\mathcal{N}_{\text{P}}}^{-1} \tilde{\mathbf{a}}_{\mathcal{N}_{\text{P}}}^i \right],$$

and we obtain an RB approximation $\tilde{A}_{\text{SC}} \tilde{\mathbf{u}}_{\text{P}} = \tilde{\mathbf{f}}_{\text{SC}}$ to the original FE truth static condensation system $A_{\text{SC}} \mathbf{u}_{\text{P}} = \mathbf{f}_{\text{SC}}$. By doing so, we need only solve $2(\mathcal{N}_{\text{P}} + 1)$ linear system of size N (to obtain the RB bubbles) and one linear system of size \mathcal{N}_{P} . If \mathcal{N} denotes the size of the complete system FE discretization, then the complexity is reduced from $\mathcal{O}(\mathcal{N}^{1+\gamma})$ ($\gamma > 0$, depending on sparsity and conditioning) to $\mathcal{O}(\mathcal{N}_{\text{P}} \times N^3 + \mathcal{N}_{\text{P}}^3)$, which is significant since typically $N \ll \mathcal{N}$ and $\mathcal{N}_{\text{P}} \ll \mathcal{N}$.

5.3. Component to system assembly. The basis functions associated with the degrees of freedom on the port P are called interface functions. We denote by ψ_k^i the restriction on Ω_i of the interface function associated with the k th degree of freedom on P . To construct ψ_k^i , we first compute the Laplacian eigenmodes χ_k on

the port domain P , and then we lift these eigenmodes in the component domains Ω_i such that they satisfy the Laplace equation.

We denote b_k^i the bubble function on Ω_i associated with the k th degree of freedom on P . The general FE solution on a subdomain Ω_i , denoted u_i , can be expressed with respect to the port coefficients \mathbf{u}_P^k as

$$(5.3) \quad u_i = \sum_{k=1}^{\mathcal{N}_P} \mathbf{u}_P^k (\psi_k^i + b_k^i).$$

We can now observe that $\mathbf{b}_k^i = A_{\Omega_i, k}^{-1} \mathbf{a}_k^i$ corresponds to the bubble equation $a_h(b_k^i, v) = -a_h(\psi_k^i, v) \forall v \in Z_h$. Furthermore,

$$A_P = (a_h(\psi_n^1 + \psi_n^2, \psi_m^1 + \psi_m^2))_{mn}$$

and

$$-A_{P, \Omega_i}^T A_{\Omega_i}^{-1} A_{P, \Omega_i} = (a_h(b_n^i, \psi_m^i))_{mn}, \quad i = 1, 2,$$

where m and n denote the row and column indices, respectively. Since functions with different superscripts do not share support, we see that we can decompose the static condensation system matrix into two static condensation component matrices, $A_{SC} = A_{SC}^1 + A_{SC}^2$, where

$$A_{SC}^i = (a_h(\psi_n^i + b_n^i, \psi_m^i))_{mn}, \quad i = 1, 2.$$

Hence, in practice, the assembly of the static condensation system is bottom-up: for each component, we assemble a local matrix A_{SC}^i , and we construct the complete static condensation matrix A_{SC} by appropriate summation of the different component matrices A_{SC}^i . The advantage of this approach is that, in many cases, several components share the same interface and bubble functions, so the assembly of A_{SC}^i can be performed only once for a group of components sharing the same parameters. In the application presented in section 6.2, this advantage holds in particular for the numerous thermal fin components.

5.4. Convection treatment. In [12], only elliptic problems are considered. In the current framework, the convection term introduces additional complexities and in particular requires special treatment at the assembly stage. In connecting the two components Ω_1 and Ω_2 , assuming the flow is from left to right, there is an interface function and associated bubble at the inlet in Ω_2 but there is none at the outlet in Ω_1 , since we consider pure convection and we do not want an artificial boundary layer at the outlet in Ω_1 .

We now describe in more detail the assembly of the two local matrices A_{SC}^1 and A_{SC}^2 . We assume that the degrees of freedom on P from 1 to $\mathcal{N}_P - 1$ correspond to the solid domain, and the degree of freedom \mathcal{N}_P is for the fluid inlet in Ω_2 . First, we consider the interface functions: for indices $1 \leq k \leq \mathcal{N}_P - 1$, the $\psi_k^i \in X_h = Y_h \times V_h$ have support only in the solid domain, and as such their component in V_h is null, and they belong to $Z_h = Y_h \times W_h$ as well. These “solid” interface functions can then serve both as trial and test functions. The last interface function $\psi_{\mathcal{N}_P}^2$ (fluid inlet degree of freedom in Ω_2) has support only in the fluid domain, and thus belongs to X_h but not necessarily to Z_h . For these reasons, we test only on the “solid” interface functions

to obtain the local component matrices

$$A_{\text{SC}}^1 = \begin{bmatrix} a_h(\psi_1^1 + b_1^1, \psi_1^1) & a_h(\psi_2^1 + b_2^1, \psi_1^1) & \cdots & a_h(\psi_{\mathcal{N}_P-1}^1 + b_{\mathcal{N}_P-1}^1, \psi_1^1) \\ \vdots & \vdots & & \vdots \\ a_h(\psi_1^1 + b_1^1, \psi_{\mathcal{N}_P-1}^1) & a_h(\psi_2^1 + b_2^1, \psi_{\mathcal{N}_P-1}^1) & \cdots & a_h(\psi_{\mathcal{N}_P-1}^1 + b_{\mathcal{N}_P-1}^1, \psi_{\mathcal{N}_P-1}^1) \end{bmatrix},$$

$$A_{\text{SC}}^2 = \begin{bmatrix} a_h(\psi_1^2 + b_1^2, \psi_1^2) & a_h(\psi_2^2 + b_2^2, \psi_1^2) & \cdots & a_h(\psi_{\mathcal{N}_P}^2 + b_{\mathcal{N}_P}^2, \psi_1^2) \\ \vdots & \vdots & & \vdots \\ a_h(\psi_1^2 + b_1^2, \psi_{\mathcal{N}_P-1}^2) & a_h(\psi_2^2 + b_2^2, \psi_{\mathcal{N}_P-1}^2) & \cdots & a_h(\psi_{\mathcal{N}_P}^2 + b_{\mathcal{N}_P}^2, \psi_{\mathcal{N}_P-1}^2) \end{bmatrix}.$$

Note A_{SC}^1 is of size $\mathcal{N}_P - 1 \times \mathcal{N}_P - 1$ and A_{SC}^2 is of size $\mathcal{N}_P - 1 \times \mathcal{N}_P$.

We now need to restore the compatibility of the two matrices, and also enforce the continuity of the fluid temperature at the port. Let ϕ_1 and ξ_k^1 be the component of u_1 and b_k^1 in V_h ; then, from (5.3), and recalling that the ‘‘solid’’ interface functions are zero in V_h , we obtain $\phi_1 = \sum_{k=1}^{\mathcal{N}_P-1} \mathbf{u}_P^k \xi_k^1$. Denoting Λ the filament coordinate of the fluid outlet in Ω_1 , we then have $\phi_1(\Lambda) = \sum_{k=1}^{\mathcal{N}_P-1} \mathbf{u}_P^k \xi_k^1(\Lambda)$. We thus modify the component matrices as follows:

$$A_{\text{SC}}^1 = \begin{bmatrix} a_h(\psi_1^1 + b_1^1, \psi_1^1) & a_h(\psi_2^1 + b_2^1, \psi_1^1) & \cdots & a_h(\psi_{\mathcal{N}_P-1}^1 + b_{\mathcal{N}_P-1}^1, \psi_1^1) & 0 \\ \vdots & \vdots & & \vdots & \vdots \\ a_h(\psi_1^1 + b_1^1, \psi_{\mathcal{N}_P-1}^1) & a_h(\psi_2^1 + b_2^1, \psi_{\mathcal{N}_P-1}^1) & \cdots & a_h(\psi_{\mathcal{N}_P-1}^1 + b_{\mathcal{N}_P-1}^1, \psi_{\mathcal{N}_P-1}^1) & 0 \\ \xi_1^1(\Lambda) & \xi_2^1(\Lambda) & \cdots & \xi_{\mathcal{N}_P-1}^1(\Lambda) & 0 \end{bmatrix},$$

$$A_{\text{SC}}^2 = \begin{bmatrix} a_h(\psi_1^2 + b_1^2, \psi_1^2) & \cdots & a_h(\psi_{\mathcal{N}_P-1}^2 + b_{\mathcal{N}_P-1}^2, \psi_1^2) & a_h(\psi_{\mathcal{N}_P}^2 + b_{\mathcal{N}_P}^2, \psi_1^2) \\ \vdots & \vdots & & \vdots \\ a_h(\psi_1^2 + b_1^2, \psi_{\mathcal{N}_P-1}^2) & \cdots & a_h(\psi_{\mathcal{N}_P-1}^2 + b_{\mathcal{N}_P-1}^2, \psi_{\mathcal{N}_P-1}^2) & a_h(\psi_{\mathcal{N}_P}^2 + b_{\mathcal{N}_P}^2, \psi_{\mathcal{N}_P-1}^2) \\ 0 & \cdots & 0 & -1 \end{bmatrix}.$$

Now both A_{SC}^1 and A_{SC}^2 are of size $\mathcal{N}_P \times \mathcal{N}_P$, and upon summing these matrices to obtain the complete system matrix A_{SC} , the last row is

$$[\xi_1^1(\Lambda) \quad \xi_2^1(\Lambda) \quad \cdots \quad \xi_{\mathcal{N}_P-1}^1(\Lambda) \quad -1].$$

Finally, we set the last coefficient in the right-hand side to zero, $\mathbf{f}_{\text{SC}}^{\mathcal{N}_P} = 0$, which will force the value of the mixed-mean temperature at the fluid inlet in Ω_2 to be equal to the value of the mixed-mean temperature at the fluid outlet in Ω_1 .

5.5. A posteriori error.

5.5.1. System port error bound. This section briefly describes a bound for the error in the system-level approximation $\|\mathbf{u}_P - \tilde{\mathbf{u}}_P\|_2$. The approach presented in [12] exploits standard RB a posteriori error estimators at the component level to develop a bound for the Frobenius norm $\|A_{\text{SC}} - \tilde{A}_{\text{SC}}\|_F$ and then applies matrix perturbation analysis at the system level to arrive at an a posteriori bound for $\|\mathbf{u}_P - \tilde{\mathbf{u}}_P\|_2$. In the current paper, we require a few variations in the general framework of [12], particularly related to the error bound for $\|A_{\text{SC}} - \tilde{A}_{\text{SC}}\|_F$. We will now present these few changes. We refer the reader interested in technical details to [12] for a complete description.

In [12], the bilinear form a is assumed to be symmetric, and by taking advantage of this property, the component matrices are symmetrized; the terms of A_{SC}^i are of the form $a_h(\psi_k^i + b_k^i, \psi_{k'}^i + b_{k'}^i)$. In our application here, due to the convection term, the bilinear form a is nonsymmetric, and instead we retain the terms of A_{SC}^i in the form $a_h(\psi_k^i + b_k^i, \psi_{k'}^i)$, as presented in the previous sections. Similarly, the coefficients of \tilde{A}_{SC}^i are of the form $a_h(\psi_k^i + \tilde{b}_k^i, \psi_{k'}^i)$, where \tilde{b}_k^i is the k th RB bubble. The error bound for $\|A_{\text{SC}} - \tilde{A}_{\text{SC}}\|_F$ is thus derived as

$$(5.4) \quad |a_h(\psi_k^i + b_k^i, \psi_{k'}^i) - a_h(\psi_k^i + \tilde{b}_k^i, \psi_{k'}^i)| = |a_h(b_k^i - \tilde{b}_k^i, \psi_{k'}^i)| \leq \gamma_0 \Delta_N^{i,k} \|\psi_{k'}^i\|_X,$$

where $\Delta_N^{i,k}$ is the standard RB error estimators for the k th bubble. To obtain the complete error bound for $\|A_{\text{SC}} - \tilde{A}_{\text{SC}}\|_F$, we also need to address the extra row which we introduced to connect the fluid channels. We directly obtain

$$(5.5) \quad |\xi_k^1(\Lambda) - \tilde{\xi}_k^1(\Lambda)| \leq \|b_k^1 - \tilde{b}_k^1\|_X \leq \Delta_N^{1,k},$$

where $\Delta_N^{1,k}$ is the standard RB error estimator for the k th bubble in Ω_1 ; this inequality is obtained since we included the term $\phi(\Lambda)^2$ in $\|u\|_X^2$ (where $u = (\theta, \phi)$).

We then sum (5.4) and (5.5) on i, k , and k' to arrive at a bound, denoted σ_2 , for the Frobenius norm $\|A_{\text{SC}} - \tilde{A}_{\text{SC}}\|_F$. All the terms in this error bound are linear with respect to the RB error bound. Due to these linear terms, we do not expect an error bound as sharp as for the symmetric case presented in [12], in which all the terms are quadratic (thanks to the assumption that a is symmetric). Note that a quadratic effect can still be obtained for nonsymmetric problems based on a primal-dual RB formulation [13], but the primal-only approach is computationally more efficient—it scales with \mathcal{N}^p instead of $(\mathcal{N}^p)^2$ —and hence, if adequate accuracy is obtained, is in fact preferred. Our final error bound is of the form

$$\|\mathbf{u}_P - \tilde{\mathbf{u}}_P\|_2 \leq \frac{\sigma_1 + \sigma_2 \|\tilde{\mathbf{u}}_P\|_2}{\tilde{\sigma}_{\min} - \sigma_2} \equiv \Delta^{\mathbf{u}_P},$$

where σ_1 is a bound for $\|\mathbf{f}_{\text{SC}} - \tilde{\mathbf{f}}_{\text{SC}}\|_2$, $\tilde{\sigma}_{\min}$ is the minimum singular value of \tilde{A}_{SC} [13], and $\|\cdot\|$ refers to the l_2 (Euclidean) norm. Of course this bound makes sense only if $\sigma_2 < \tilde{\sigma}_{\min}$.

5.5.2. System output error bound. We now consider as an output of our system a quantity defined over the port domain and which can be defined as a linear functional of the system solution \mathbf{u}_P . In our case, such outputs can be simply the value of the solution at a particular point in the fluid domain, or the solution average over the port in the solid domain. We can write the FE output as $s = \mathbf{m}^T \mathbf{u}_P$, with $\mathbf{m} \in \mathbb{R}^{\mathcal{N}_P}$, and the corresponding RB output as $\tilde{s} = \mathbf{m}^T \tilde{\mathbf{u}}_P$. We next introduce the adjoint $\mathbf{z} \in \mathbb{R}^{\mathcal{N}_P}$ solution of

$$\tilde{A}_{\text{SC}}^T \mathbf{z} = -\mathbf{m}.$$

Recalling that $A_{\text{SC}} \mathbf{u}_P = \mathbf{f}_{\text{SC}}$ and $\tilde{A}_{\text{SC}} \tilde{\mathbf{u}}_P = \tilde{\mathbf{f}}_{\text{SC}}$, we obtain the matrix perturbation equation

$$(5.6) \quad \tilde{A}_{\text{SC}} \delta \mathbf{u}_P = \delta \mathbf{f}_{\text{SC}} - \delta A_{\text{SC}} \tilde{\mathbf{u}}_P - \delta A_{\text{SC}} \delta \mathbf{u}_P,$$

where $\delta \mathbf{u}_P = \mathbf{u}_P - \tilde{\mathbf{u}}_P$, $\delta \mathbf{f}_{\text{SC}} = \mathbf{f}_{\text{SC}} - \tilde{\mathbf{f}}_{\text{SC}}$, and $\delta A_{\text{SC}} = A_{\text{SC}} - \tilde{A}_{\text{SC}}$. Multiplication of (5.6) from the left by $\mathbf{m}^T \tilde{A}_{\text{SC}}^{-1} = -\mathbf{z}^T$ yields

$$(5.7) \quad s - \tilde{s} = -\mathbf{z}^T \delta \mathbf{f}_{\text{SC}} + \mathbf{z}^T \delta A_{\text{SC}} \tilde{\mathbf{u}}_P + \mathbf{z}^T \delta A_{\text{SC}} \delta \mathbf{u}_P.$$

We now bound each term on the right-hand side of (5.7) to obtain a bound for $|s - \tilde{s}|$. First, we directly obtain

$$|\mathbf{z}^T \delta A_{\text{SC}} \tilde{\mathbf{u}}_{\text{P}}| \leq \sum_{i,j \text{ over port dof}} |\mathbf{z}^i| |\delta A_{\text{SC}}^{ij}|_{\text{bound}} |\tilde{\mathbf{u}}_{\text{P}}^j| \equiv \varepsilon_{A_{\text{SC}}},$$

where $|\delta A_{\text{SC}}^{ij}|_{\text{bound}}$ refers to the bound on the Schur complement entry RB error given by (5.4) and (5.5). A similar bound $\varepsilon_{\mathbf{f}_{\text{SC}}}$ can be obtained for $|\mathbf{z}^T \delta \mathbf{f}_{\text{SC}}|$ as

$$|\mathbf{z}^T \delta \mathbf{f}_{\text{SC}}| \leq \sum_{i \text{ over port dof}} |\mathbf{z}^i| |\delta \mathbf{f}_{\text{SC}}^i|_{\text{bound}} \equiv \varepsilon_{\mathbf{f}_{\text{SC}}};$$

note that in our particular application, $\delta \mathbf{f}_{\text{SC}} = \mathbf{f}_{\text{SC}} = \tilde{\mathbf{f}}_{\text{SC}} = 0$. To bound the last term on the right-hand side of (5.7) we appeal to the system port error bound presented in the previous section,

$$|\mathbf{z}^T \delta A_{\text{SC}} \delta \mathbf{u}_{\text{P}}| \leq \|\mathbf{z}\|_2 \sigma_2 \Delta^{\text{up}} = \varepsilon_{\text{quad}},$$

where we recall that the l_2 norm is bounded by the Frobenius norm.

Hence our final output error bound is

$$\Delta^s = \varepsilon_{\mathbf{f}_{\text{SC}}} + \varepsilon_{A_{\text{SC}}} + \varepsilon_{\text{quad}};$$

it follows from our derivation that $|s - \tilde{s}| \leq \Delta^s$. This output error bound is much sharper than the simple result, which can be derived from continuity arguments, $\|\mathbf{m}\|_2 \Delta^{\text{up}}$. First, Δ^{up} is presumably pessimistic because the Frobenius norm in σ_2 is too strong; in contrast, the $\varepsilon_{A_{\text{SC}}}$ term should be relatively sharp—we miss only sign cancellation. Second, the factor $\frac{1}{\tilde{\sigma}_{\text{min}} - \sigma_2}$ in Δ^{up} does not appear in the terms $\varepsilon_{\mathbf{f}_{\text{SC}}}$, and $\varepsilon_{A_{\text{SC}}}$; $\frac{1}{\tilde{\sigma}_{\text{min}} - \sigma_2}$ in Δ^{up} can be quite large because $\tilde{\sigma}_{\text{min}}$ can be small and furthermore σ_2 can be close to $\tilde{\sigma}_{\text{min}}$. Note that the bound Δ^{up} is still a factor in $\varepsilon_{\text{quad}}$, but now premultiplied by σ_2 , which mitigates the impact.

The term $\varepsilon_{\text{quad}}$ is hence quadratic in the error bounds since it involves the product $\sigma_2 \Delta^{\text{up}}$. As a consequence, it should be negligible compared to $\varepsilon_{\mathbf{f}_{\text{SC}}} + \varepsilon_{A_{\text{SC}}}$ for a sufficiently good RB approximation. We may then consider the following simple output error indicator (not rigorous):

$$\overline{\Delta}^s \equiv \varepsilon_{\mathbf{f}_{\text{SC}}} + \varepsilon_{A_{\text{SC}}}.$$

This error indicator is interesting from a computational point of view since by eliminating $\varepsilon_{\text{quad}}$ we do not need to compute Δ^{up} , and hence we avoid computation of the minimum singular value of \tilde{A}_{SC} . For large systems where \mathcal{N}_{P} is large (typically $\mathcal{N}_{\text{P}} > 10^6$), the minimum singular value computation can become prohibitive, especially in a many-query or real-time context. The error indicator $\overline{\Delta}^s$ is thus an interesting alternative to the error bound Δ^s when considering large systems.

6. Numerical examples. All the results presented in this section were obtained using `rb00mit` [16] and `libMesh` [15].

6.1. Model problem (1D). We first consider a 1D version of our problem for which we can find a closed-form solution, and which thus permits us to compare our method to a ground truth. To this end, we set the solid domain to be 1D: $\Omega = [0, \Lambda]$.

In this case, we can reduce our problem (2.1) to a system of ODEs (see Appendix A) where both θ and ϕ are defined on $[0, \Lambda]$:

$$(6.1) \quad \begin{cases} -\theta'' + \text{Bi}_{\text{ext}}\theta + \text{Bi}_{\text{int}}(\theta - \phi) = f, \\ \mathcal{F}\phi' - \text{Bi}_{\text{int}}(\theta - \phi) = 0. \end{cases}$$

We impose the following boundary conditions: $\theta'(0) = 0$, $\theta'(\Lambda) = 0$, and $\phi(0) = 0$.

For the values $\text{Bi}_{\text{ext}} = 1$, $\text{Bi}_{\text{int}} = \frac{6}{5}$, $\mathcal{F} = 1$, $f = 1$ (we do not require $\mathcal{F} \geq 2$ in the 1D case), a particular solution of the system (6.1) (without imposition of boundary conditions) is $\theta = 1$, $\phi = 1$; the set of solutions to the homogeneous system is

$$\begin{cases} \theta(x) = 2Ae^{-2x} + 45Be^{\frac{2+\sqrt{19}}{5}x} + 45Ce^{\frac{2-\sqrt{19}}{5}x}, \\ \phi(x) = -3Ae^{-2x} + (48 - 6\sqrt{19})Be^{\frac{2+\sqrt{19}}{5}x} + (48 + 6\sqrt{19})Ce^{\frac{2-\sqrt{19}}{5}x}, \end{cases} \quad A, B, C \in \mathbb{R}.$$

The values for A, B, C are then chosen such that the solution satisfies the boundary conditions. We show in Figure 3 the graphs of θ and ϕ for $\Lambda = 4$.

We now solve the same problem numerically for a system of four components, each of unity length. We show in Figure 4a the error in the H^1 norm between the FE static condensation and the analytical solution. We observe that the error is $\mathcal{O}(h)$, as predicted by our a priori error estimate. We now consider RB bubble approximations: we consider $(\text{Bi}_{\text{ext}}, \mathcal{F}) \in [0.33, 3]^2$ as the parameters of the system of ODEs (6.1), and we construct RB spaces using the standard Greedy algorithm [20] for $N \leq N_{\text{max}} \equiv 15$ modes (these RB approximations are built on a “truth” FE approximation with a uniform mesh of size $h = 0.002$). We consider for the output the fluid temperature at the outlet, corresponding to $s = \phi(4)$. The output error $|s - \tilde{s}|$ between the FE static condensation and the RB static condensation is shown in Figure 4b; we also indicate the primal output error bound ($\|\mathbf{m}\|_2 \Delta^{\text{up}}$), the dual output error bound (Δ^s), and the dual output error indicator ($\overline{\Delta}^s$), all presented in section 5.5. The effectivity is about 10^3 for the primal error bound, and 10^2 for the dual error bound; the latter thus provides about one order of magnitude improvement. We also observe that $\overline{\Delta}^s$ converges very rapidly to Δ^s , which confirms our assumption that the term $\varepsilon_{\text{quad}}$ becomes negligible for a sufficiently good RB approximation.

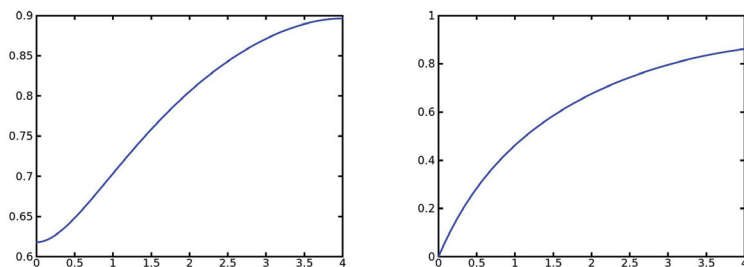


FIG. 3. Graphs of θ (left) and ϕ (right) for the simple test case on $[0, 4]$. Boundary conditions are homogeneous Neumann for θ and $\phi(0) = 0$.

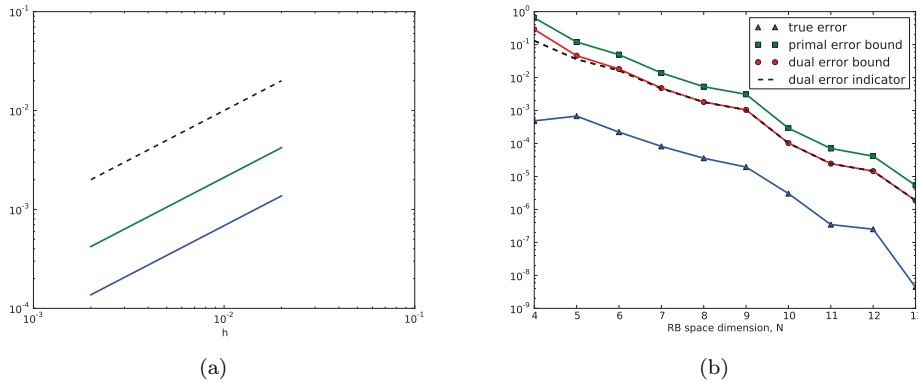


FIG. 4. (a) Static condensation FE error with respect to the analytical solution: blue, error in $H^1([0, \Lambda])$ of θ ; green, error in $H^1([0, \Lambda])$ of ϕ ; the dashed line indicates a slope of unity. (b) scRBE error with respect to static condensation FE.

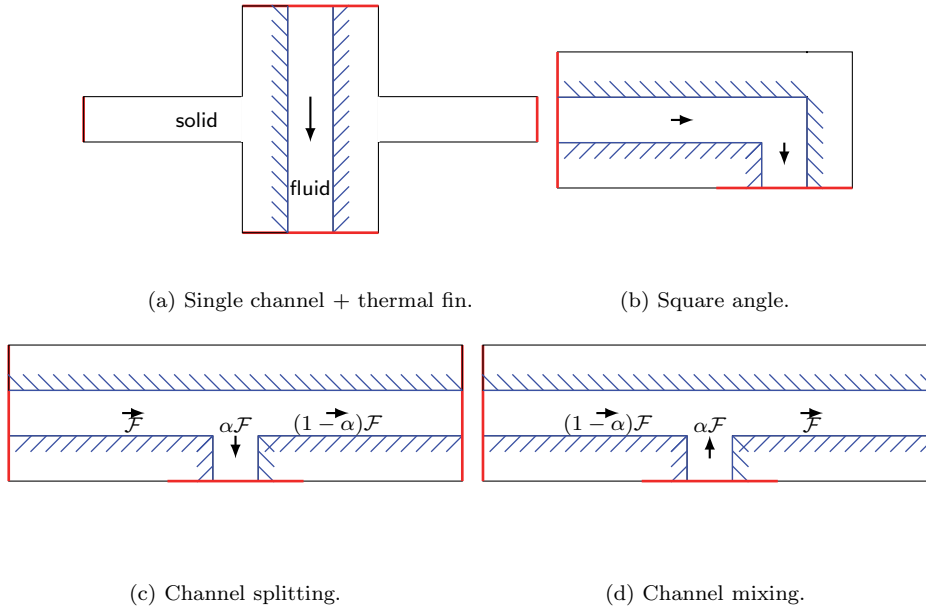
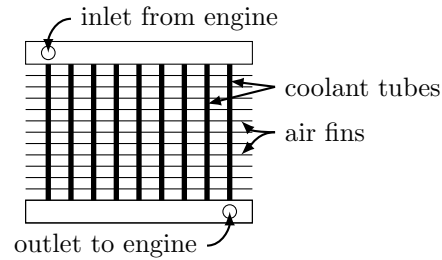


FIG. 5. The component library. Components can be connected at the ports shown in red.

6.2. Simple automotive radiator. We now consider the library of components shown in Figure 5. All these components are based on the various models presented in the previous sections. We can now assemble many such components to model an automotive radiator as shown in Figure 6.

We need to consider parameter values that make sense for a radiator. First, we consider the parameter \mathcal{F} and we assume the following values for purposes of estimation: the flow rate of coolant through the radiator can vary greatly, from 1 liter/min for economical cars to more than 100 liter/min for sport cars ($1 \text{ kg/min} \leq \rho\bar{v}\mathcal{A} \leq 100 \text{ kg/min}$ for water); the flow is divided equally among 30 coolant tubes; a coolant duct has a rectangular section of $1 \text{ mm} \times 10 \text{ mm}$ ($\mathcal{P} = 22 \text{ mm}$, $\mathcal{A} = 10 \text{ mm}^2$),

FIG. 6. *Automotive radiator.*

and is modeled as a 2D channel of hydraulic diameter $\mathcal{D} = \frac{4A}{P} = 1.82$ mm; the radiator is made of aluminium ($k = 250\text{W}/(\text{m}\cdot\text{K})$); the coolant is water ($c = 4.2\text{kJ}/(\text{kg}\cdot\text{K})$, $k_f = 0.6\text{W}/(\text{m}\cdot\text{K})$ at 100°C). Since $\mathcal{F} = \frac{\rho c \bar{v} A}{P k}$, we obtain that $0.4 \leq \mathcal{F} \leq 40$ in the coolant tubes. In the following numerical results, we limit the range of the parameter \mathcal{F} to $[2, 40]$. It is important to note that for this range of \mathcal{F} , we obtain a Reynolds number $Re = \frac{\rho \bar{v} \mathcal{D}}{\mu} \in [1700, 34000]$, which justifies our model preference for a turbulent flow.

We then consider Bi_{int} . For turbulent flow, from the Gnielinski correlation, we obtain a Nusselt number in the range $10 \leq Nu \leq 150$. Since $Nu = \frac{h_{\text{int}} \mathcal{D}}{k_f}$, where \mathcal{D} is the diameter of the channel and k_f is the heat conductivity of the fluid, we obtain $\text{Bi}_{\text{int}} = Nu \frac{\mathcal{W}}{\mathcal{D}} \frac{k_f}{k}$. Assuming that $\frac{\mathcal{W}}{\mathcal{D}} \simeq 1$, it follows that $0.025 \leq \text{Bi}_{\text{int}} \leq 0.4$.

Finally, for parameter Bi_{ext} corresponding to the Biot number of the aluminium-air heat exchange, we assume the following values: the air flow velocity along the radiator fins varies from 10 m/s to 30 m/s, the distance between two fins is 10 mm, and the length of a fin from tube to tube is 20 mm, which corresponds to a hydraulic diameter of 13 mm for the duct created by two parallel fins. For these values and air properties at 20°C , the Gnielinski correlation gives a Nusselt number in the range $[25, 60]$. This corresponds to the range $[2 \times 10^{-4}, 5 \times 10^{-4}]$ for Bi_{ext} . Since in our examples we consider small radiators with far fewer fins than actual radiators, we will consider higher values of Bi_{ext} , in the range $[0.01, 0.1]$, so that we can obtain a more significant heat exchange.

In all of the following, the RB is trained on the previously defined range of parameters, except Bi_{int} is fixed in all cases to 0.1. The online computations can thus be performed for any parameters $[\mathcal{F}, \text{Bi}_{\text{ext}}, \text{Bi}_{\text{int}}] \in D$ with $D = [2, 40] \times [0.01, 0.1] \times \{0.1\}$. For mixing and splitting components we consider the additional parameter α in the domain $[0.1, 0.9]$. We use RB spaces of maximum dimension $N_{\text{max}} = 30$.

We will now consider a set of examples for a radiator with five coolant tubes and five fins per tube (35 components), as shown in Figure 7a. As a boundary condition, we will always set the (nondimensional) fluid bulk temperature at the inlet equal to 1. As the output of interest, s , we will consider the fluid exit temperature at the radiator outlet. We will consider different scenarios by varying the parameters \mathcal{F} and Bi_{ext} to demonstrate the design flexibility of our approach, as well as the accuracy of the error bound for the output. Note that in practice the flow distribution in the coolant tubes would be determined from some simple “head loss” hydraulic model, but here we directly specify the flow rates in the different channels: we conserve mass and invoke symmetry or homogeneity as appropriate.

For the first scenario, we choose $\text{Bi}_{\text{ext}} = 0.02$ and $\text{Bi}_{\text{int}} = 0.1$ throughout the

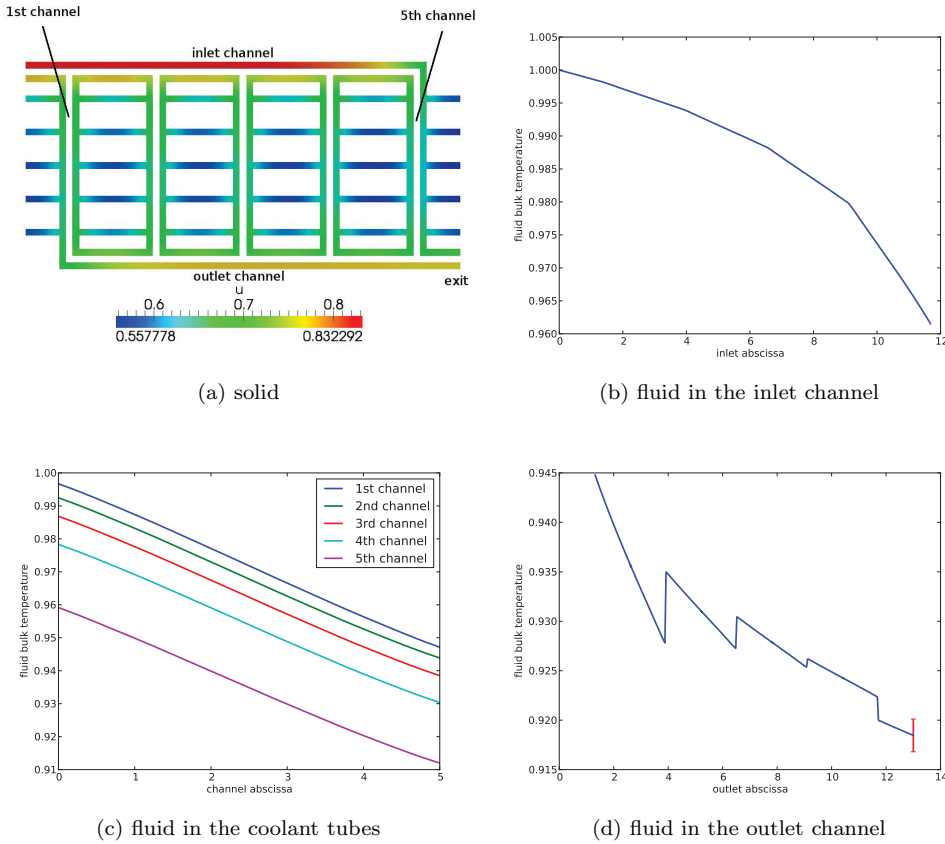


FIG. 7. Temperature field in the system: $Bi_{\text{ext}} = 0.02$ and $Bi_{\text{int}} = 0.1$; $\mathcal{F} = 15$ at the inlet, $\mathcal{F} = 3$ in each coolant tube. The red error bar corresponds to the error bound Δ^s for the fluid temperature at the exit of the heat exchanger. The jumps in temperature in the outlet channel are due to mixing components.

whole system. The flow rate at the entrance is $\mathcal{F} = 15$, and then splits so that it is equal to 3 in each tube. The temperature in the solid domain is shown in Figure 7a. In the inlet channel (Figure 7b), the fluid bulk temperature decreases more rapidly after each channel splitting, because the flow rate in the inlet channel diminishes after each splitting. In the coolant tubes (Figure 7c), the fluid bulk temperature decreases at the same rate for all tubes, because the parameters Bi_{ext} and Bi_{int} are the same everywhere, and hence the overall heat transfer coefficient is the same for all tubes. In the outlet channel (Figure 7d), the fluid bulk temperature jumps after each channel mixing, which is expected due to our mixing model described in section 4.1. Finally, at the exit, the fluid bulk temperature is 0.918. The absolute error $|s - \tilde{s}|$ of the fluid exit temperature is 1.3×10^{-6} , and the error bound Δ^s is 1.6×10^{-3} : RB prediction for the fluid temperature at the exit is certified to incur an error of at most 0.17% with respect to the FE prediction.

It is important to note the improvement obtained with the new output dual error bound Δ^s . Indeed, the primal port error bound at the exit $\|\mathbf{m}\| \Delta^{\text{up}}$ is 0.19, corresponding to an effectivity of 10^5 . (Comparatively, the primal error bounds reported

in [12] have effectivities of 10^2 . This very large difference in effectivities is anticipated in section 5.5.1 and is due to the linear versus quadratic effect in the RB bubble error bounds.) But thanks to the new output dual error bound, Δ^s , a better effectivity (10^3 here) and a useful error bound can be recovered. Also, the dual error indicator $\overline{\Delta}^s$ in this case is 1.2×10^{-3} , which is different from, but still rather close to, $\Delta^s = 1.6 \times 10^{-3}$.

As a second scenario, we consider the fact that, in actual practice, it is unlikely that all coolant tubes will have the same flow rate, especially if some tubes are obstructed, corroded, or bent. We retain $\text{Bi}_{\text{ext}} = 0.02$ and $\text{Bi}_{\text{int}} = 0.1$ throughout the whole system, but we now modify the flow rates in the coolant tubes: the flow rate at the entrance is still $\mathcal{F} = 15$, but it then splits as $\mathcal{F} = 5$ in the first coolant tube, $\mathcal{F} = 4$ in the second, and $\mathcal{F} = 2$ in all other coolant channels. As a consequence, we can see in Figure 8b that the fluid bulk temperature decreases more in coolant tubes with the lowest flow rate. However, after the mixing of all coolant tubes, the exit temperature is almost the same as in the first scenario (0.919). The flow distribution in the coolant tubes does not have a significant effect on the exit temperature here. Due to the fact that we use the same RB spaces, the output error and output error bound are almost exactly the same as for the first scenario.

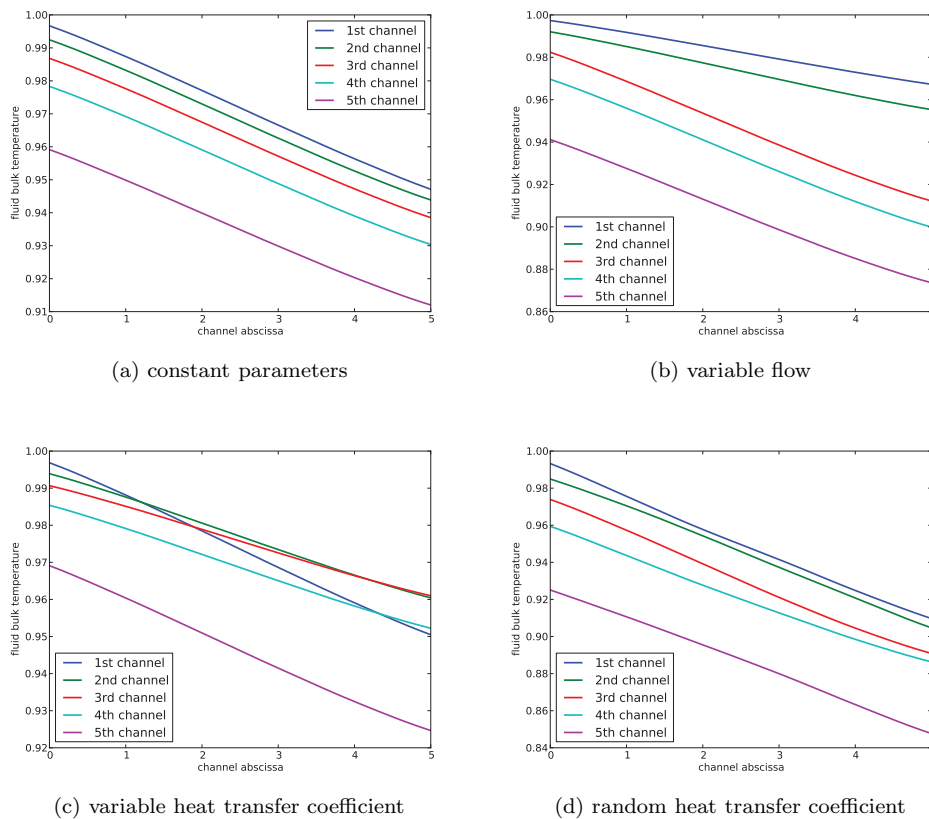


FIG. 8. Fluid bulk temperature in the channels for different scenarios. Note all figures refer to the radiator configuration of Figure 7a.

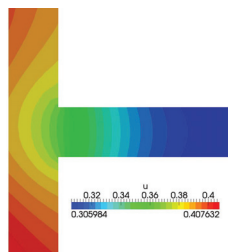


FIG. 9. *Temperature field: expanded view of a fin in the solid domain.*

For the third scenario, we consider the common situation in which the fins are dirty with mud or insects and the heat transfer coefficient is correspondingly compromised. Thus in this example we take $\text{Bi}_{\text{ext}} = 0.02$ and $\text{Bi}_{\text{int}} = 0.1$ throughout the whole system *except* for the three middle “dirty” coolant channels for which we choose a smaller value, $\text{Bi}_{\text{ext}} = 0.01$. The flow rate at the entrance is $\mathcal{F} = 15$, and then splits so that it is equal to 3 in each tube. We can see in Figure 8c that the fluid bulk temperature decreases less in the three middle coolant tubes due to a smaller overall heat transfer coefficient. This time the outlet temperature is significantly higher (0.938), confirming that the heat exchanger does not perform as well as in the previous cases.

For the fourth and last scenario, we illustrate the many-parameter and heterogeneous capabilities of our method. We take $\text{Bi}_{\text{int}} = 0.1$ throughout the whole system, but we select random values of Bi_{ext} for each component independently, in the range $[0.01, 0.1]$. The flow rate at the entrance is $\mathcal{F} = 15$, and then splits so that it is equal to 3 in each tube. In Figure 8d we observe that the temperature in the coolant tubes decreases at a variable rate due to the variability of the heat transfer coefficient.

Finally, we show in Figure 9 an expanded view of the temperature distribution in the base of a fin for the first scenario (the case depicted in Figure 7a). We can see the restriction effect near the base of the fin where the temperature field is 2D, followed by the low-Biot largely 1D temperature distribution within the fin itself. This visualization emphasizes why our detailed 2D PDE model in the solid is important.

We conclude with a much larger system, now with 20 coolant channels and 20 fins per channel (440 components in total), in order to illustrate the computational savings of the scRBE method. The parameters Bi_{ext} and Bi_{int} are chosen to be 0.02 and 0.1, respectively, throughout the whole system. The flow rate at the entrance is $\mathcal{F} = 40$, and then splits so that it is equal to 2 in each tube. The outlet temperature is 0.679 and the error bound Δ^s is 5.5×10^{-3} , which corresponds to an error of at most 0.8% between the RB and FE exit temperature. The quality of the error bound decreases compared to the previous examples, as expected since we are summing the RB bubble error bounds over many more components (440 instead of 35).

The computational timings are the following: the assembly of the FE static condensation system requires 12 minutes whereas the assembly of the RB static condensation system takes 1.1 seconds, corresponding to a speedup factor of 500. The resulting static condensation system is of dimension $\mathcal{N}_{\mathcal{P}} = 8500$ and is solved in 0.05 seconds; it is important to mention that although the Schur complement matrix has dense blocks between coupled ports, globally there is much sparsity, which can be taken advantage of when solving the static condensation system. We can also compare the scRBE cost to an FE solution with all degrees of freedom (before condensation): in this case, the number of system degrees of freedom is 3×10^5 . To estimate the cost of the system

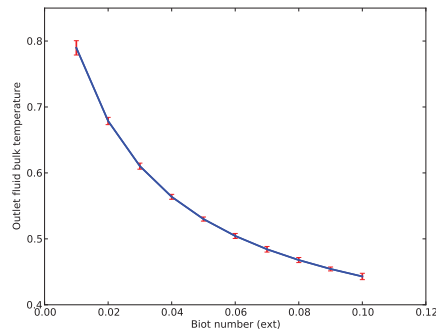


FIG. 10. Exit temperature with respect to Bi_{ext} for a system with 20 coolant channels and 20 fins per channel. The error bounds (Δ^s) are shown as red error bars.

FE approach, we solve a 2D Laplacian on a square with 3×10^5 FE degrees of freedom: the assembly time is 1.5 seconds, and the solution time is 4 minutes. Hence, compared to the system FE approach, the scRBE speed up is a factor of 210. We now turn to the error bound. The predominant cost is the computation of the minimal singular value $\tilde{\sigma}_{\min}$ —about 10 seconds. We thus see the computational advantage of the error indicator $\overline{\Delta}^s$, which only requires the solution of an adjoint problem of the same size as the primal problem—hence 0.05 seconds. In this example we obtain $\overline{\Delta}^s = 3.4 \times 10^{-3}$, quite close to $\Delta^s = 5.5 \times 10^{-3}$.

It should be noted that other computational savings can be obtained. First, in the previous timings we did not take advantage of repeated subdomains which share the same parameters, such as the 400 fin components in the present example. It is possible to perform the RB evaluation only once for all these fin components, and in this case the RB static condensation assembly time drops to less than 0.01 s. Second, we can truncate the Laplacian eigenmode expansion for the degrees of freedom at the ports in order to reduce \mathcal{N}_P —often without any significant loss in accuracy of the method. These computational aspects are discussed in detail in [12, 5].

Finally, we show in Figure 10 the outlet temperature (in our large system of 20 channels) as the parameter Bi_{ext} is varied from 0.01 to 0.1 (for all components of the system). This result demonstrates the design potential of the scRBE and the certification afforded by the error bounds.

Appendix. 1D problem. If Ω is a rectangular domain, and we take the limit as $\mathcal{W} \rightarrow 0$ (the width of the solid domain), then $Bi_{\text{ext}} \rightarrow 0$, $Bi_{\text{int}} \rightarrow 0$, and the solution of (2.1) and (2.2) becomes independent of the y coordinate in the solid. In fact, as $\mathcal{W} \rightarrow 0$, the PDE (2.1) tends to the following ODEs in which both θ and ϕ are defined on $[0, \Lambda]$:

$$(A.1) \quad \begin{cases} -\theta'' + Bi_{\text{ext}}\theta + Bi_{\text{int}}(\theta - \phi) = f, \\ \mathcal{F}\phi' - Bi_{\text{int}}(\theta - \phi) = 0. \end{cases}$$

We can hence consider (A.1) as the 1D version of our original 2D problem (2.1). Since this 1D limit is valid as Bi tends to zero, we should then take Λ large in order to observe any appreciable temperature decay; however, for the purpose of our simple numerical test in section 6.1, we consider order unity Bi and Λ . We will summarize in this appendix the few differences between the 1D problem and the 2D problem.

We denote $I = [0, \Lambda]$. The trial space is $X = H_0^1(I) \times V$, where $V = \{\phi \in H^1(I) | \phi(0) = 0\}$, and the test space is $Z = H_0^1(I) \times L^2(I)$. The weak form reads as follows: find $u \in X$ such that $a(u, v) = f(v) \forall v \in Z$, where

$$(A.2) \quad \begin{aligned} & a(w, v) \\ &= \int_I \frac{d\theta}{dx} \frac{d\vartheta}{dx} + \text{Bi}_{\text{ext}} \int_I \theta \vartheta + \text{Bi}_{\text{int}} \int_I (\theta - \phi) \vartheta - \text{Bi}_{\text{int}} \int_I (\theta - \phi) \varphi + \mathcal{F} \int_I \frac{d\phi}{dx} \varphi. \end{aligned}$$

Looking at stability, we obtain

$$(A.3) \quad \begin{aligned} a(w, w^*) &\geq \int_I \left(\frac{d\theta}{dx} \right)^2 + \left(\text{Bi}_{\text{ext}} - \frac{1}{2} \tau \frac{\text{Bi}_{\text{int}}^2}{\mathcal{F}} \right) \int_I \theta^2 \\ &\quad + \frac{1}{2} \tau \mathcal{F} \int_I \left(\frac{d\phi}{dx} \right)^2 + \frac{1}{2} (\mathcal{F} + \tau \text{Bi}_{\text{int}}) \phi^2(\Lambda) \\ &\geq K(\tau) \|w\|_X^2 \end{aligned}$$

for τ small enough. We can take

$$(A.4) \quad \text{Bi}_{\text{ext}} - \frac{1}{2} \tau \frac{\text{Bi}_{\text{int}}^2}{\mathcal{F}} = 0 \iff \tau = \frac{2\text{Bi}_{\text{ext}}\mathcal{F}}{\text{Bi}_{\text{int}}^2}$$

so that the second term in the right-hand side of (A.3) vanishes: $a(\cdot, \cdot)$ is then inf-sup stable from the same arguments provided in the 2D case. The form $a(\cdot, \cdot)$ is also continuous. The methodology for FE and RB approximations then proceeds as in the 2D case.

Acknowledgement. We would like to acknowledge helpful discussions with Dr. David Knezevic of Harvard and Dr. Phuong Huynh of MIT.

REFERENCES

- [1] G.S. BAROZZI AND G. PAGLIARINI, *A method to solve conjugate heat transfer problems: The case of fully developed laminar flow in a pipe*, J. Heat Transfer, 107 (1985), pp. 77–83.
- [2] P. BINEV, A. COHEN, W. DAHMEN, R. DEVORE, G. PETROVA, AND P. WOJTASZCZYK, *Convergence rates for greedy algorithms in reduced basis methods*, SIAM J. Math. Anal., 43 (2011), pp. 1457–1472.
- [3] A. BUFFA, Y. MADAY, A.T. PATERA, C. PRUD'HOMME, AND G. TURINICI, *A priori convergence of the greedy algorithm for the parametrized reduced basis method*, ESAIM Math. Model. Numer. Anal., 46 (2012), pp. 595–603.
- [4] R. CRAIG AND M. BAMPION, *Coupling of substructures for dynamic analyses*, AIAA J., 6 (1968), pp. 1313–1319.
- [5] J.L. EFTANG AND A.T. PATERA, *Port reduction in component-based static condensation for parametrized problems: Approximation and a posteriori error estimation*, Int. J. Numer. Meth. Eng., 96 (2013), pp. 269–302.
- [6] A. ERN AND J.L. GUERMOND, *Theory and Practice of Finite Elements*, Appl. Math. Sci. 159, Springer-Verlag, New York, 2004.
- [7] A. ERN, S. PEROTTO, AND A. VENEZIANI, *Hierarchical model reduction for advection-diffusion-reaction problems*, Numerical Mathematics and Advanced Applications, 2008, pp. 703–710.
- [8] A.G. FEDOROV AND R. VISKANTA, *Three-dimensional conjugate heat transfer in the microchannel heat sink for electronic packaging*, Int. J. Heat Mass Transfer, 43 (2000), pp. 399–415.
- [9] L. FORMAGGIA, J.F. GERBEAU, F. NOBILE, AND A. QUARTERONI, *On the coupling of 3d and 1d Navier-Stokes equations for flow problems in compliant vessels*, Comput. Methods Appl. Mech. Engrg., 191 (2001), pp. 561–582.
- [10] V. GNIELINSKI, *New equations for heat and mass transfer in turbulent pipe and channel flow*, Int. Chem. Eng., 16 (1976), pp. 359–368.

- [11] W. C. HURTY, *On the Dynamic Analysis of Structural Systems Using Component Modes*, in First AIAA Annual meeting, Washington, D.C., AIAA paper 64-487, 1964.
- [12] D.B.P. HUYNH, D.J. KNEZEVIC, AND A.T. PATERA, *A static condensation reduced basis element method: Approximation and a posteriori error estimation*, ESAIM Math. Model. Numer. Anal., 47 (2013), pp. 213–251.
- [13] D.B.P. HUYNH, D.J. KNEZEVIC, AND A.T. PATERA, *A static condensation reduced basis element method: Complex problems*, Comput. Methods Appl. Mech. Engrg., 259 (2013), pp. 197–216.
- [14] D.B.P. HUYNH, G. ROZZA, S. SEN, AND A.T. PATERA, *A successive constraint linear optimization method for lower bounds of parametric coercivity and inf-sup stability constants*, C. R. Math. Acad. Sci. Paris, 345 (2007), pp. 473–478.
- [15] B. S. KIRK, J. W. PETERSON, R. H. STOGNER, AND G. F. CAREY, *libMesh: A C++ library for parallel adaptive mesh refinement/coarsening simulations*, Eng. Comput., 22 (2006), pp. 237–254.
- [16] D. J. KNEZEVIC AND J. W. PETERSON, *A high-performance parallel implementation of the certified reduced basis method*, Comput. Meth. Appl. Mech. Eng., 200 (2011), pp. 1455–1466.
- [17] J. H. LIENHARD IV AND J. H. LIENHARD V, *A Heat Transfer Textbook*, 4th ed., Phlogiston Press: Cambridge, Massachusetts, 2011.
- [18] Y. MADAY AND E.M. RØNQUIST, *The reduced basis element method: Application to a thermal fin problem*, SIAM J. Sci. Comput., 26 (2004), pp. 240–258.
- [19] S. PEROTTO, A. ERN, AND A. VENEZIANI, *Hierarchical local model reduction for elliptic problems: A domain decomposition approach*, Multiscale Model. Simul., 8 (2010), pp. 1102–1127.
- [20] C. PRUD’HOMME, D. ROVAS, K. VEROY, Y. MADAY, A.T. PATERA, AND G. TURINICI, *Reliable real-time solution of parametrized partial differential equations: Reduced-basis output bounds methods*, J. Fluids Eng., 124 (2002), pp. 70–80.
- [21] W. QU AND I. MUDAWAR, *Analysis of three-dimensional heat transfer in micro-channel heat sinks*, Int. J. Heat Mass Transfer, 45 (2002), pp. 3973–3985.
- [22] A. QUARTERONI AND A. VALLI, *Numerical Approximation of Partial Differential Equations*, Springer-Verlag, Berlin, 2008.
- [23] G. ROZZA, D. B. P. HUYNH, AND A. T. PATERA, *Reduced basis approximation and a posteriori error estimation for affinely parametrized elliptic coercive partial differential equations: Application to transport and continuum mechanics*, Arch. Comput. Methods Eng., 15 (2008), pp. 229–275.
- [24] G. ROZZA AND K. VEROY, *On the stability of the reduced basis method for Stokes equations in parametrized domains*, Comput. Methods Appl. Mech. Engrg., 196 (2007), pp. 1244–1260.
- [25] K. VEROY, C. PRUD’HOMME, D. V. ROVAS, AND A. T. PATERA, *A Posteriori error bounds for reduced-basis approximation of parametrized noncoercive and nonlinear elliptic partial differential equations*, in Proceedings of the 16th AIAA Computational Fluid Dynamics Conference, 2003, paper 2003-3847.
- [26] A. WEISBERG, H. H. BAU, AND J. N. ZEMEL, *Analysis of microchannels for integrated cooling*, Int. J. Heat Mass Transfer, 35 (1992), pp. 2465–2474.